Velocity bunching of high-brightness electron beams

S. G. Anderson,[1,*] P. Musumeci,[2] J. B. Rosenzweig,[2] W. J. Brown,[1] R. J. England,[2] M. Ferrario,[3] J. S. Jacob,[1] M. C. Thompson,[2] G. Travish,[2] A. M. Tremaine,[1] and R. Yoder[2]

[1]*Lawrence Livermore National Laboratory, 7000 East Avenue, Livermore, California 94550, USA*

[2]*Department of Physics and Astronomy, University of California, Los Angeles, 405 Hilgard Avenue, Los Angeles, California 90095, USA*

[3]*Istituto Nazionale di Fisica Nucleare, Laboratori Nazionali di Frascati, 41 Via Enrico Fermi, Frascati (Roma), Italy*

(Received 28 April 2004; published 18 January 2005)

Velocity bunching has been recently proposed as a tool for compressing electron beam pulses in modern high brightness photoinjector sources. This tool is familiar from earlier schemes implemented for bunching dc electron sources, but presents peculiar challenges when applied to high current, low emittance beams from photoinjectors. The main difficulty foreseen is control of emittance oscillations in the beam in this scheme, which can be naturally considered as an extension of the emittance compensation process at moderate energies. This paper presents two scenarios in which velocity bunching, combined with emittance control, is to play a role in nascent projects. The first is termed ballistic bunching, where the changing of relative particle velocities and positions occur in distinct regions, a short high gradient linac, and a drift length. This scenario is discussed in the context of the proposed ORION photoinjector. Simulations are used to explore the relationship between the degree of bunching, and the emittance compensation process. Experimental measurements performed at the UCLA Neptune Laboratory of the surprisingly robust bunching process, as well as accompanying deleterious transverse effects, are presented. An unanticipated mechanism for emittance growth in bends for highly momentum chirped beam was identified and studied in these experiments. The second scenario may be designated as phase space rotation, and corresponds closely to the recent proposal of Ferrario and Serafini. Its implementation for the compression of the electron beam pulse length in the PLEIADES inverse Compton scattering (ICS) experiment at LLNL is discussed. It is shown in simulations that optimum compression may be obtained by manipulation of the phases in low gradient traveling wave accelerator sections. Measurements of the bunching and emittance control achieved in such an implementation at PLEIADES, as well as aspects of the use of velocity-bunched beam directly in ICS experiments, are presented.

DOI: 10.1103/PhysRevSTAB.8.014401 PACS numbers: 41.60.Ap, 29.27.Bd, 52.59.Sa

I. INTRODUCTION

Recently, the demand for applications of high brightness–low emittance, high current, with subpicosecond (subps) pulse length—electron beams has increased dramatically [1–4]. Such applications are found in advanced accelerators; for example, the source injection requirements for short wavelength, high gradient accelerators demand ultrashort pulses of very low emittance. Additionally, relatively high charge, subps electron beams are required for driving plasma wakefield accelerators. In the fourth generation synchrotron light source community, high-brightness beams are needed for application to short wavelength self-amplified spontaneous emission free-electron lasers (SASE FEL), as well as for inverse-Compton-scattering (ICS) generation of short x-ray pulses. Recent designs of systems capable of delivering high brightness very short electron beams have included the use of conventional photoinjectors in conjunction with magnetic compressors [2]. While magnetic compression schemes have proven successful in increasing the beam current, their impact on the transverse phase space has been shown not to be benign. When performing the compression at low energy, both velocity-field and centrifugal space-charge forces are not yet strongly suppressed by the relativistic cancellation of electric and magnetic fields, and their emittance-damaging effect becomes significant, during bends [5,6]. In the case of compression at higher energy, there can be deleterious effects on the longitudinal as well as the transverse phase space of coherent synchrotron radiation (CSR) [7–10]. Both longitudinal and transverse phase space filamentation, and associated emittance growth, run counter to the goal of increasing the beam brightness that motivates the use of compression to begin with. An alternative scheme that may preserve the transverse phase space quality, while compressing the beam to subps bunch length, has been proposed by Serafini and Ferrario (SF) [11]. This scheme, commonly known as "velocity bunching"—opposed to the path-length dependence of magnetic compression systems—is an extension of the commonly employed technique of rf rectilinear compression. As design trajectory bending is not needed in this system, one may avoid the phase space degrading effects observed in magnetic compression experiments on photoinjector-derived beams [5,6]. Velocity bunching has been typically used to bunch dc electron sources at kinetic

*Electronic address: anderson131@llnl.gov

energies in the 100's of keV range. It has also been used in rf photoinjectors beginning in a similarly low-energy region very close to photocathode [12,13] by injection of the electron bunch far ahead of the rf crest. The scheme of SF, however, does not begin the bunching until the beam has exited the rf photocathode gun, and the initial emittance compensation (first plasma oscillation) has been completed. The bunching then occurs at energies above several MeV, during postacceleration and the second and final transverse plasma oscillation, which produces the ultimate compensation of the emittance. The simultaneous action of velocity bunching and emittance compensation has been initially studied by SF; it is examined in further detail using simulations and experiments in two different scenarios in this paper. It should be emphasized that velocity bunching allows for the compression to occur early in the acceleration process, at a lower energy than magnetic compression. This attribute plays a strong motivating role for the implementation of velocity bunching in the two applications discussed in the following sections. In the first application, to the ORION photoinjector, we examine the use of velocity bunching to compress bunches emitted from an *S*-band (2.856 MHz) rf gun, using a high gradient, short *S*-band linac section as a buncher. This scheme, which operates in a ballistic bunching regime where the compression occurs mainly in a drift, is needed to shorten the bunch length from one characteristic of the *S*-band gun to one scaled appropriately to the *X*-band linacs which give the majority of the total acceleration in the ORION photoinjector. One may control the phase spread of the beam at the lowest possible energy, thus mitigating the beam's final energy spread. This scenario, which is critical to the ORION facility mission, will be elaborated upon further below. The other experimental scheme we present here is the velocity bunching scenario employed at the PLEIADES (Picosecond Laser-Electron Interaction for Dynamic Evaluation of Structures) ICS experiment located at LLNL. In this experiment, one simultaneously strives for short bunches, in order to achieve shorter pulse x rays through electron beam pulse compression, and low energy spread, to obtain smaller—not as severely chromatic aberration limited—electron beam spot sizes in the beam's final focus system. The photoinjector system in this case is an *S*-band rf gun that is nearly identical to the ORION gun, followed by four *S*-band traveling wave (TW) linear accelerator (linac) sections. This layout is similar in most respects to the original SF proposal, with some notable exceptions that are discussed below in the context of simulations. As the velocity-based compression occurs not within a drift, but inside of a linac, we term this variant of velocity bunching "phase space rotation," in which the synchrotron motion is mediated by continuous application of rf acceleration forces. To motivate the reported experiments at Neptune Laboratory and at the LLNL PLEIADES photoinjector, we will review two design studies. The ORION velocity-bunching scheme will form the background of the Neptune experiments, while the PLEIADES design study directly underpins our understanding of the experiment itself. The ORION study is unique, in that it is the first to propose and study the "thin-lens" version of velocity bunching and associated emittance compensation. The PLEIADES study, in addition to its experimental relevance, illuminates the role of using slower than light-speed phase velocity structure that SF have proposed. In order to place the present work in the correct context, one must review the previous experiments in which velocity bunching has been employed in high brightness rf photoinjectors. At the BNL ATF Laboratory, bunching has been observed [12,13] in a 1.6 cell *S*-band rf gun when the electron beam is launched from the cathode at phases, in standard rf gun convention, far below 90°. This effect has been shown to produce modest compression of beams, and is based on both phase space rotation within the gun, and ballistic bunching after the gun. Furthermore, it was consistent with achieving good emittance behavior. The use of this type of velocity bunching is limited, however, by the constraints simultaneously placed on the photoemission, acceleration, focusing, and space-charge handling aspects of the system. The SF proposal allows more flexibility in velocity bunching, by moving the onset of the compression process to the entrance of the first linac section, after the initial emittance compensation. It thus separates the functions of producing an initially optimized beam, and subsequent compression. Further, in order to preserve the emittance during velocity bunching, the SF scheme proposes use of external focusing solenoids around the linac sections. This allows for tuning of the beam sizes and associated emittance oscillations during velocity bunching and postacceleration. Recently, a set of experiments have been performed [14] at the BNL SDL Laboratory, in a layout which may approximate, from the longitudinal dynamics viewpoint, the low energy component (first two 3-m linac sections) of the SF scheme. In these measurements, agreement was found between simulation and experimental determination of the bunch length, with a minimum rms pulse length of 0.6 ps. Because no solenoid focusing was available at the SDL linac, however, the issues of transverse beam size and emittance control were not addressed experimentally. In contrast, in the LLNL phase space rotation experiments discussed here, solenoids are used to optimize the transverse emittance during the bunching process. Further, the compressed beams, having rms pulse lengths as short as 0.3 ps, are used in ICS experiments, providing a demonstration of the utility of the SF scheme of velocity bunching. It should be noted that the ATF version of velocity bunching has been used as a tool for creating shorter bunches for a variety of applications. The present results obtained at PLEIADES show much more dramatic compression in this first use of the SF velocity scheme in application than previously

obtained. The Neptune experiments are discussed in the context of their relevance to the ORION ballistic bunching proposal. As there is no postacceleration after the bunching, the Neptune measurements may be considered as a first test of the initial half of the ORION-type velocity bunching. In addition, in the process of measuring the ''slice'' beam dynamics using a bend magnet, these experiments have led to the identification of a new mechanism—based on a subtle understanding of the longitudinal-transverse correlations in the system—that drives emittance growth in bends.

II. BALLISTIC BUNCHING AT THE ORION PHOTOINJECTOR

The ORION photoinjector [15], which is now under construction as a joint SLAC/UCLA project, has at its core a 1.6 cell *S*-band (2.856 MHz) rf gun, which is to be operated at high gradient, 120–140 MV/m peak on-axis field. The emittance compensation process proceeds as in the now-standard LCLS design [16], with a beam being focused by a solenoid directly after the gun, through a 1.4 m drift, to the initial linac. Unlike the LCLS case, however, the linacs, which run at moderately high acceleration gradient (33 MeV/m average), are *X*-band devices. Nevertheless, these 11.424 GHz linac sections are equipped with a series of independently powered solenoid coils, and thus one may choose a solenoid field which allows operation on the invariant envelope, which optimizes emittance compensation [17]. Thus, excellent emittance performance is expected in this scenario, about 0.3 mm mrad at the nominal design charge of 0.25 nC. Because of the scaling of beam size inherent in the *S*-band gun, however, the energy spread due to the phase spread in the *X*-band structures may be too large for some experiments. The most relevant example is laser acceleration, in which the needed energy resolution is very small, on the level of 100 keV or less. In order to achieve ultrasmall energy resolution with a velocity-bunching scheme in the ORION injector, we have studied the inclusion of a short 0.42 m bunching section placed at the same initial position, 1.5 m downstream of the cathode, as the first *X*-band linac in the nominal design [15]. This positioning guarantees that the initial emittance oscillation is identical to that in the optimized LCLS-type design. The bunching linac is taken in the simulations to be an *S*-band plane-wave transformer (PWT) linac of the type installed at the Neptune Lab [18]. The two *X*-band linac sections are moved downstream 1 m, allowing for the ballistic bunching of the beam in a 0.6 m drift after the PWT, as shown schematically in Fig. 1.

In Fig. 1, the results of a HOMDYN [16] slice-envelope simulation show the evolution of the rms bunch length and relative momentum spread of a 10 pC beam. It can be seen that the longitudinal dynamics in this case are well optimized for laser acceleration experiments at the ORION photoinjector, with a final state of 20 μm rms bunch length, and less than 0.2% residual rms energy spread ($<$ 100 keV). The transverse dynamics are not modeled well by HOMDYN in this case, and are discussed further below in the context of multiparticle simulations. This scenario is but one of many where velocity bunching should be considered at the ORION photoinjector. Another is the case where one desires very high peak currents, for studying plasma wakefield excitation. This mode of operation has been studied using UCLA PARMELA, in order to explore the issue of emittance compensation during the compression process illustrated in Fig. 1. As PARMELA is a multiparticle, instead of a slice-envelope, code, it is capable of modeling the transverse phase space evolution of the beam in detail. The results of this study are shown in Figs. 2–7, which display the case of a 1 nC beam. Figures 2 and 3 indicate the overall parameters that control the evolution of the longitudinal and transverse dynamics, respectively. In Fig. 2, we display the normalized mean energy γ of the beam as a function of distance along the beam line z; note that the PWT bunching linac is run 10° ahead of the zero crossing, and the beam is actually decelerated on average. This is necessary because of the strong dependence of the bunching process on average energy, and on space-charge forces. To quantify this dependence, we note that the drift one must use to remove an initial chirp $d(\delta p/p)/d\zeta$ (where $\zeta = z - vt$ is longitudinal distance measured in the beam frame) is

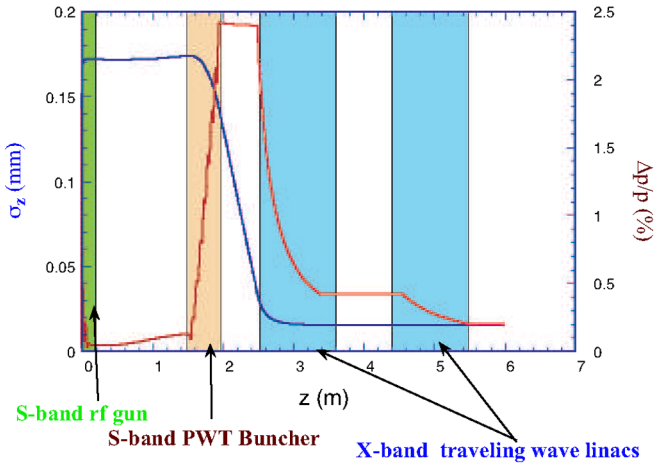

FIG. 1. (Color) HOMDYN simulation of the rms bunch length and relative momentum spread for a 10 pC case, optimized for laser acceleration experiments at the ORION photoinjector. The rms bunch length, plotted in blue, begins to decrease inside of the *S*-band buncher and continues though the drift space, finally reaching a minimum value of 20 μm inside of the first *X*-band linac section. In contrast, the relative, rms momentum spread, plotted in red, increases sharply in the buncher and is subsequently decreased by acceleration in the two *X*-band sections to a final value of 0.2%.

$$L_d = \frac{\gamma^3}{\frac{d(\delta p/p)}{d\zeta}}. \quad (1)$$

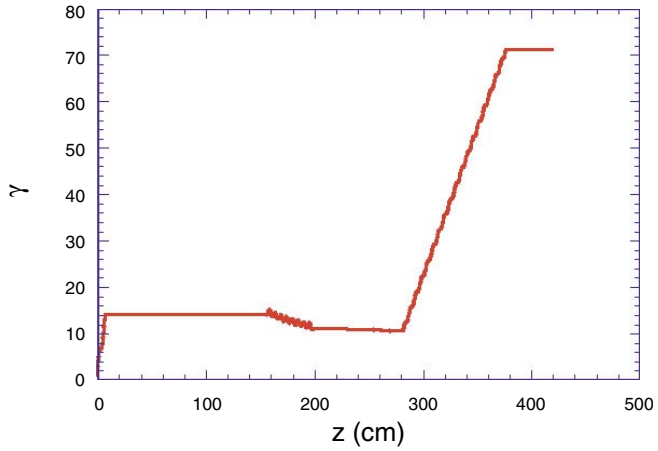

FIG. 2. (Color) The evolution of the normalized beam energy for 1 nC beam in the ORION photoinjector, velocity-bunching case, from PARMELA simulation.

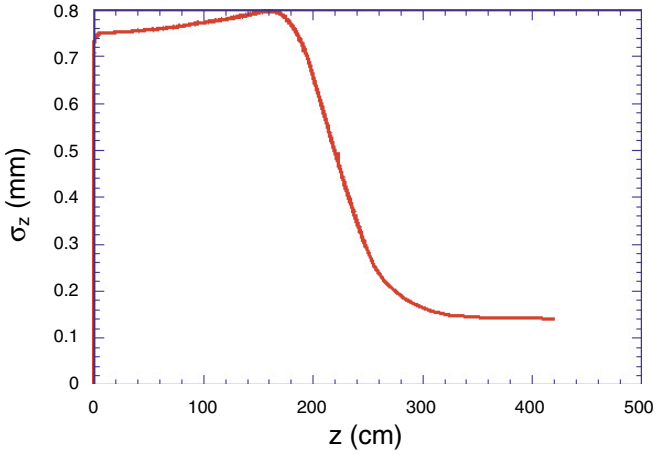

FIG. 4. (Color) Evolution of the rms bunch length for 1 nC beam in the ORION photoinjector, velocity-bunching case, from PARMELA simulation.

The chirp after the bunching linac is related to that before it, $d(\delta p/p)/d\zeta|_0$, by

$$\frac{d(\delta p/p)}{d\zeta} = \frac{d(\delta p/p)}{d\zeta}\bigg|_0 + k_{\rm rf}\frac{\Delta p_m}{p_0}\left[\frac{\sin\phi}{1+\frac{\Delta p_m}{p_0}\cos\phi}\right]. \tag{2}$$

Here p_0 is the beam momentum after the gun, Δp_m is the maximum momentum gain available in the linac, the rf wave number is defined as $k_{\rm rf} = 2\pi/\lambda_{\rm rf}$, and the rf phase $\phi = k_{\rm rf}(z - vt) + \phi_0$ has the opposite sign convention of the gun phase mentioned above. With the longitudinal dynamics established, the transverse beam dynamics then are controlled by adjusting the solenoid amplitude and its spatial profile. As the ORION photoinjector X-band traveling wave linacs inherit the Next Linear Collider Test Accelerator injector focusing solenoids overlaid upon the acceleration region, one may use these existing magnets to achieve a tailoring of the longitudinal magnetic field profile. The optimized field profile which produces good emittance compensation at the exit of the first X-band linac section is shown in Fig. 3.

For the parameters of the ORION design [$p_0 = 7$ MeV/c, $\Delta p_m = 14$ MeV/c, $d(\delta p/p)/d\zeta|_0 = 14$ m^{-1}], the drift from the bunching linac to longitudinal focus is predicted to be approximately 0.8 m. In fact, it is a bit longer than this, as can be seen in Figs. 2 and 4, because of the defocusing effects of longitudinal space-charge forces. It can be seen in Fig. 4 that the longitudinal focusing is arrested by acceleration in the X-band linac after bunching from 800 μm rms down to 150 μm. The compressed bunch length is limited from below by both nonlinearities in the (sinusoidal) rf accelerating waveform, and by space-charge forces. Explicit manifestations of these collective forces are displayed in the longitudinal phase space shown in Fig. 6

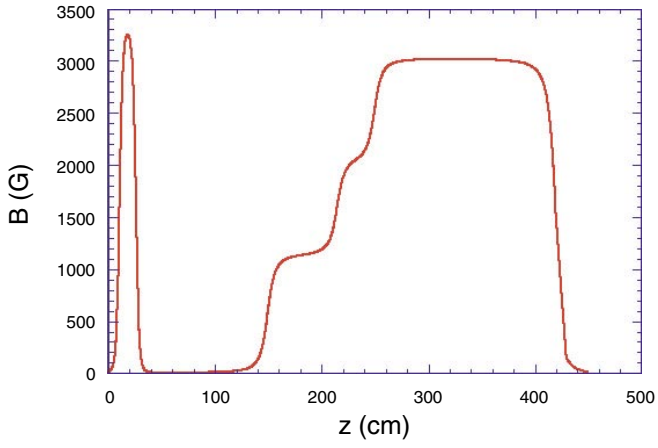

FIG. 3. (Color) The z dependence of the longitudinal magnetic field used in the PARMELA simulation of the ORION photoinjector.

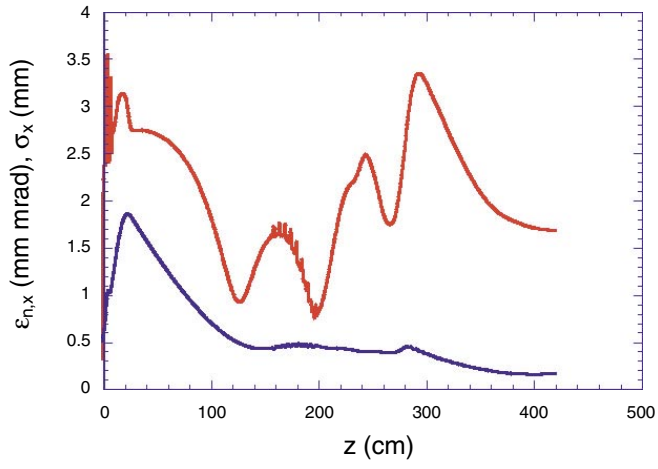

FIG. 5. (Color) Evolution of the rms transverse beam size and emittance for 1 nC beam in the ORION photoinjector, velocity-bunching case, from PARMELA simulation.

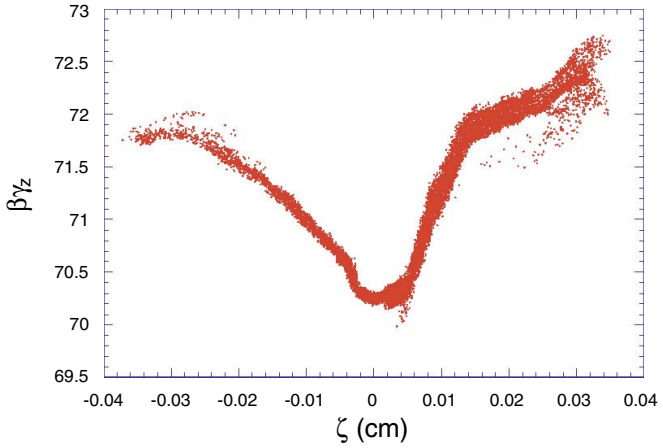

FIG. 6. (Color) Evolution of the rms transverse beam size and emittance for 1 nC beam in the ORION photoinjector, velocity-bunching case, from PARMELA simulation.

The z dependences of the beam's transverse rms size and emittance, as predicted by PARMELA, are shown in Fig. 5. It can be seen that the increase in the beam current (to above 1 kA) associated with compression causes the control of the beam emittance oscillations to become more difficult. These oscillations show characteristic increased frequency as the beam-plasma frequency grows with higher current, and also display a secular trend upward. This secular behavior could have been anticipated from previous theoretical work on phase space evolution in near-equilibrium situations, in which wave breaking of the transverse phase space distribution and associated emittance growth occur [19,20]. It should be noted also that the case shown in Figs. 2–5 is one in which the beam does not undergo wave breaking (crossover) in longitudinal phase space, as can be seen in the PARMELA simulation results displayed in Fig. 6.

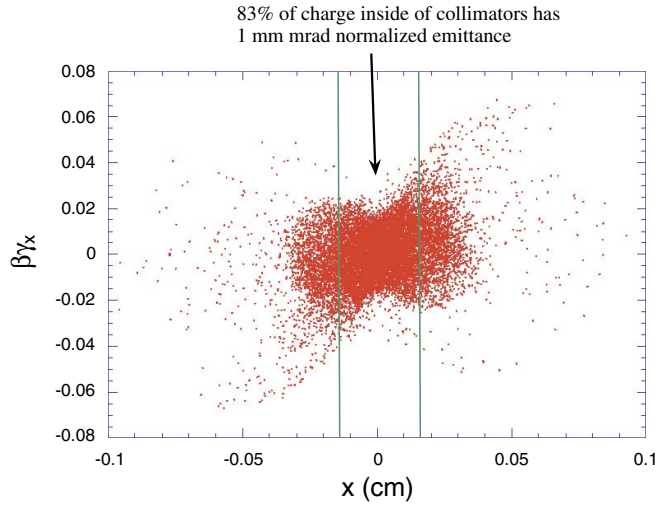

FIG. 7. (Color) Evolution of the rms transverse beam size and emittance for 1 nC beam in the ORION photoinjector, velocity-bunching case, from PARMELA simulation.

Under crossover conditions, different longitudinal slices of the original beam are allowed to overlap. This results, as in the case of magnetic compression, in strong emittance growth due to the enhanced amplitude and nonlinearity of the transverse space-charge fields [6].

Even in the absence of longitudinal crossover, the secular transverse emittance growth over the series of emittance oscillations is non-negligible, and leads to development of a halo [21] of large amplitude particles. This halo may be dealt with by cutting the distribution which, upon removal of only 17% of the particles using horizontal collimation, gives a reduction of the normalized emittance from 1.7 to 1.0 mm mrad.

From this discussion, we see that there are numerous experimental questions concerning this ballistic bunching scheme, with most arising from the effects of space-charge forces. From the viewpoint of longitudinal space charge, one may search for a signature of minimum achievable bunch length and accompanying momentum spread, if not a complete characterization of the longitudinal phase space. With respect to transverse forces, one should study the effects of space charge in the various regions: ballistic drift, accelerator, and/or solenoid. With these studies in hand, one may more confidently address the full process of maintaining emittance compensation during velocity bunching. It will be seen that not all of these goals could be addressed in the test bed we have used to explore the ballistic regime. Our available experimental configuration is that of the Neptune photoinjector at UCLA, which contains a 1.6 cell gun and a PWT standing wave linac; these are the same first two rf devices in the ORION ballistic bunching system. This system has no postacceleration or solenoid focusing after the PWT buncher, thus limiting the range of experimental questions that can be addressed. Nevertheless, significant experimental progress in understanding the ballistic bunching scheme was accomplished. In the following sections we review the experimental scheme employed, give experimental results, and compare the results to computational models. The investigations that could be undertaken at Neptune were mainly centered on measurement of the bunch length using the coherent transition radiation (CTR) interferometry. Parametric studies of linac electric field amplitude in the bunching linac were performed, allowing determination of the best compressing phase for different acceleration gradients. A partial investigation of transverse dynamics relevant to the ORION scheme was undertaken. The presence of strong chirping of the beam means that one may use a dispersing dipole to select a portion of the beam with a relatively small energy spread, thus allowing longitudinal slice measurements of the beam. In this way, the emittance of the central slice of the electron beam was studied via quad scan techniques. As the phase of the rf accelerating wave in the PWT approached the optimum compression conditions, emittance growth was observed. We present

three-dimensional simulations that agree well with the experimental results. The interpretation of this experimental scenario has some subtlety, however, and a novel effect that can introduce an unanticipated emittance growth in the bend is thus discussed.

III. NEPTUNE EXPERIMENTAL LAYOUT

The Neptune facility at UCLA is operated both as an injector for an advanced accelerator experiments such as plasma beat-wave acceleration [22] and as a test bed for high-brightness beam dynamics studies. These studies have included emittance growth in bends [6] and negative R_{56} compressors [23] for production of shaped beams that may be employed as optimum plasma wakefield drivers. The Neptune photoinjector [18] and associated laboratory measurement capabilities [24] are therefore well suited for ballistic compression studies. The layout of the beam line is shown schematically in Fig. 8. The photoinjector beam in these experiments is created initially by a 266 nm wavelength, 6 ps rms long laser pulse impinging on a single crystal copper cathode inside of a 1.6 cell rf gun. The photoelectrons generated are then accelerated by the rf fields of peak on-axis amplitude $\sim$80 MV/m, and are transversely focused into the PWT linac entrance using the emittance compensation solenoid. At this point the beam can be energy chirped for ballistic bunching inside the 8-cell, 42 cm long, *S*-band PWT rf cavity that is run forward of crest (maximum acceleration). There is independent control and measurement of the phases of the two accelerating structures, as is needed for testing the ballistic bunching scheme. Downstream of the linac there is an insertable aluminum foil to generate coherent transition radiation, which is collected by a parabolic mirror and reflected to a Martin-Puplett autocorrelator used as a pulse length diagnostic. There are also four dipoles along the beam line that may be used as a magnetic chicane compressor (not of direct use in these experiments), or if only the final two magnets are used to bend (45° total) in the same direction, as a spectrometer. For the ballistic bunching experiments, a quadrupole lens and a Ce:YAG screen are employed after the 45° bend, for slice-emittance measurements employing quad scanning.

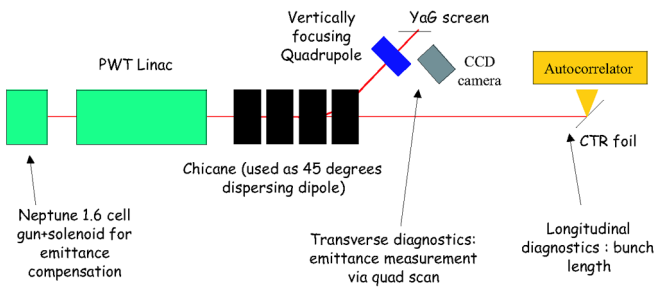

FIG. 8. (Color) Schematic layout of the Neptune ballistic bunching experiment.

IV. LONGITUDINAL DYNAMICS IN THE BALLISTIC BUNCHING EXPERIMENT

The ballistic bunching in the Neptune experiments is described well by the approximate relations given in Eqs. (1) and (2). Because one compresses with ballistic bunching by running the PWT far from crest (+ 70°), and near the zero crossing, the final bunch length is not as strongly limited by rf nonlinearity as in magnetic compression [2] or phase space rotation, where the beam manipulations require application of rf fields having strong longitudinal curvature near to the wave crest. Additionally, since the beam is not well-focused transversely after the PWT, the effects of longitudinal space charge are not as notable at Neptune as in the ORION case. As shown below, very short beams can be created by use of this scheme.

The pulse length in these measurements is determined by use of coherent transition radiation interferometry using a polarizing Martin-Puplett interferometer. The resolution of the interferometer is limited by the spectral response of the two wire grid polarizers: the grids do not efficiently reflect wavelengths shorter than the wire separation distance of 100 μm. As for long wavelengths, the analysis of the interferometer data must take into account the loss of such components in the CTR spectrum due to inefficient creation of the CTR due to finite target size, subsequent diffraction of long wavelengths, and vacuum window transmission. These effects are all dealt with in analysis using a frequency filtering algorithm that uses a fit to the time-domain data [25]. We note that since the CTR measurement is performed on a moderately relativistic beam, the radiation divergence ($\approx 1/\gamma$) cone of the radiation is quite large. Because the Martin-Puplett is a polarizing interferometer, and because the polarization of transition radiation depends on the direction of propagation, care was taken to mitigate the effects of misalignment and resultant losses in the collection of CTR, as they can result in systematic errors in the measurement.

For a case with approximately $Q \approx 250$ pC of charge, injected 70° off crest in the PWT cavity (optimal compression), we obtain the interferogram shown in Fig. 9.

The time-domain filtered fit to the data gives an rms pulse length of 0.39 ps. It is worth noting the compressed beam is shorter than that achieved using magnetic compression at Neptune [6] (over 0.6 ps) with similar beam charge and slightly shorter initial bunch length. This observation confirms the role of the linearity of the rf wave in compression, which is generally the limiting factor in the final achievable pulse length [2]. It is also interesting to see that the Neptune beam was compressed to a length 35% shorter than achieved in the BNL velocity bunching experiments [14]; further, the compression factor (12–15) is much larger than in the BNL measurements (approximately 3).

The predictions for optimum bunching conditions given in Eqs. (1) and (2) have been experimentally tested by

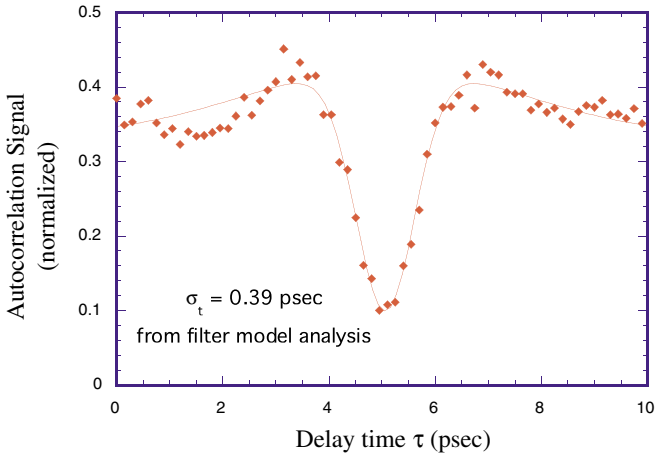

FIG. 9. (Color) Autocorrelation of optimally compressed beam in Neptune ballistic bunching experiment, with time-domain fit analysis.

measuring the phase ϕ of best compression, while changing the energy gradient in the PWT. The rf-cavity phase was measured by mixing the rf fields inside the structure with a reference rf clock, while the phase for maximum compression was determined by maximizing the CTR energy interferometer Golay-cell detectors. Maximizing the CTR minimizes the bunch length, since the coherent energy scales with the inverse bunch length [26], $E_{\mathrm{CTR}} \propto Q^2/\sigma_t$. A comparison between the measured data and the analytical approximation is within the experimental uncertainties, as seen in Fig. 10.

The higher uncertainties in the measurement for higher gradient indicate that the system is increasingly sensitive to rf phase noise when higher gradients are used for bunching.

With the calibration of rf, beam charge, and launch dimensions known, one may also compare aspects of the

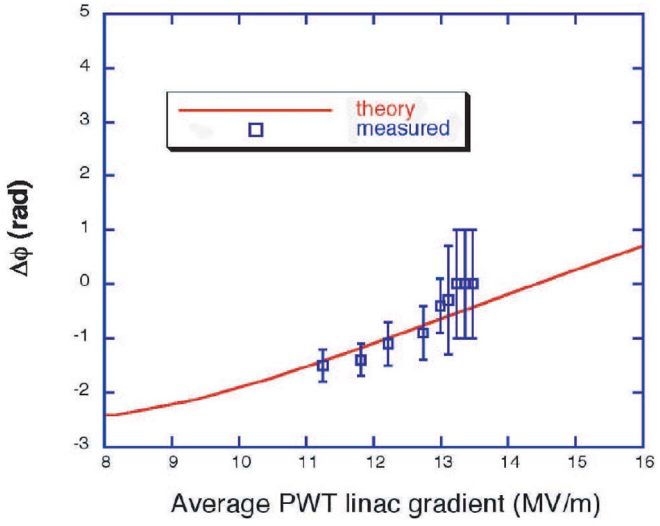

FIG. 10. (Color) Maximum bunching phase in PWT versus PWT accelerating gradient, theory and measurement.

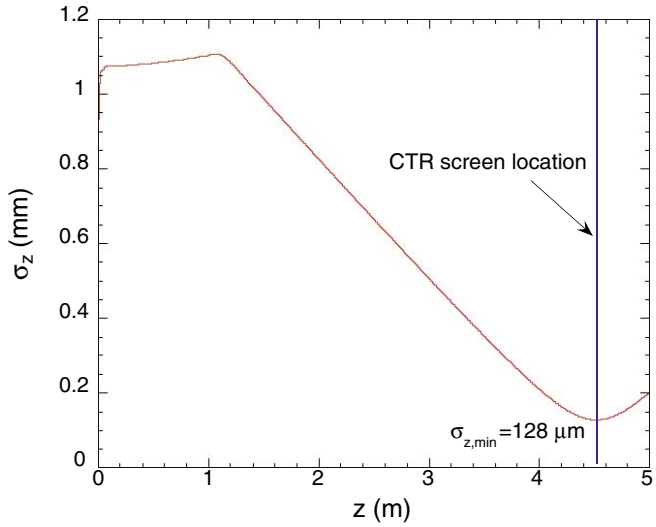

FIG. 11. (Color) Evolution of rms bunch length in Neptune ballistic bunching experiment, showing minimum of $\sigma_{z,\mathrm{min}} = 128\ \mu$m near CTR measurement screen location for experimental conditions.

measurements with more complete models of the beam dynamics. Figure 11 shows the results of a HOMDYN simulation of the conditions of the Neptune experiment, for the calibrated rf linac phase of 70°, $\sigma_{z,\mathrm{min}} = 128\ \mu$m.

The minimum achieved rms bunch length deduced from the CTR measurement is 117 μm, in quite good agreement. Note that the simulation indicates a compression of the beam by 1 order of magnitude, as does the comparison of measured photocathode laser pulse length with the measured electron beam $\sigma_{z,\mathrm{min}}$.

V. TRANSVERSE DYNAMICS IN THE BALLISTIC BUNCHING EXPERIMENT

The results of Sec. IV confirm that ballistic bunching can be an efficient way of increasing the peak current of the beam, which was raised from roughly 17 A to over 250 A in the experiment. The remaining question is: what is the damage to the emittance during this compression process, which has no downstream beam focusing or postacceleration?

As the initial energy of the beam upon entrance to the PWT buncher is low, 4.2 MeV, it is not necessary to run forward of the rf zero crossing; for optimal compression the beam runs through the high gradient structure 70° off crest, still in the roughly linearly changing part of the rf wave. Under these conditions, the energy spread at the exit of the PWT is large. For example, in the case in which the focus of the longitudinal lens is 3 m downstream of the PWT, and the rf phase is set 70° off crest, the resulting energy spectrum extends from 5 to 9 MeV. This would not be an inherent problem in a system where the beam energy can be boosted up by additional accelerating cavities to quickly remove the relative energy spread, but at the

Neptune photoinjector there is no such capability. This limits the methods for determining the transverse projected emittance, because the energy spread may appear, e.g., in trace space quad scan measurements, as unphysical transverse emittance arising from severe chromatic aberrations.

On the other hand, the energy is correlated with the longitudinal position within the beam. If a small window in energy is accepted in a given measurement, a longitudinal slice of the beam can be selected. Experimentally, a 45° bend dipole was employed to *horizontally* disperse the beam momenta, and then a beam slice was selected, over which a *vertical* quad scan emittance measurement was performed. With this method we have studied the vertical phase space of the longitudinal core of the electron beam, scanning the phase of the linac to understand the transverse dynamics of the beam as it was undergoing compression.

Changing the linac phase, which is the variable that controls the compression, also causes changes in the energy spectrum of the beam. On the other hand, it is important to ensure that the same longitudinal slice of the beam impinges on the quad scan detection screen. The screen subtends several degrees of bending angle, corresponding to $\approx 2\%$ of energy spread. In order to be able to set the dipole current to keep the same portion of the beam at the 45° bend angle as the overall energy changes, we first measure the full energy spectrum as the linac phase is changed, then select one reference slice. We chose the central slice (maximum charge, as determined by a Faraday cup in the bend line), and the dipole is adjusted to keep this slice in the analysis window.

In Fig. 12 one observes energy change of this central reference slice of the beam as the linac phase is varied. This curve also allows an independent determination of the rf cavities' accelerating gradients. We deduce from fitting this rf phase scan data that the energy gain in the 1.6 cell gun is 4.2 MeV, corresponding to a peak on-axis gradient of 80 MV/m, and the gain in the PWT is 8.4 MeV, corresponding to a 40 MV/m peak on-axis accelerating gradient.

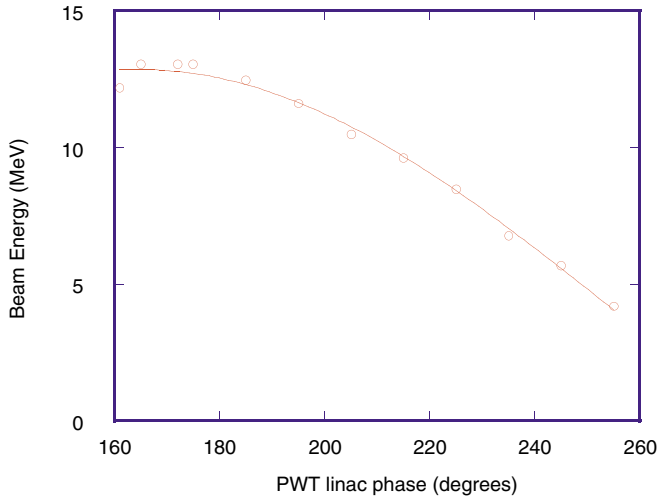

FIG. 12. (Color) Energy of central slice, measured versus the phase of the linac, as determined by maximum Faraday cup signal. Energy fit to data has assumed functional form $E = E_{\text{gun}} + E_{\text{PWT}} \sin(\phi + \phi_0)$.

Once the central reference beam slice is found, the quad scan is performed to determine the emittance in the vertical dimension. Since the beam varies in size significantly going through the quad, an analysis that takes into account the thickness of the quadrupole lens is needed. The parametrization of the square of the measured beam size with respect to the quad strength is

$$\begin{aligned}\sigma^2(K) = {} & [\cos(\sqrt{K}l_q) - \sqrt{K}l_d \sin(\sqrt{K}l_q)]^2\sigma_{11} \\ & + 2\left[\frac{\sin(\sqrt{K}l_q)}{\sqrt{K}} + l_d\cos(\sqrt{K}l_q)\right][\cos(\sqrt{K}l_q) \\ & - \sqrt{K}l_d\sin(\sqrt{K}l_q)]\sigma_{12} + \left[\frac{\sin(\sqrt{K}l_q)}{\sqrt{K}}\right. \\ & \left. + l_d\cos(\sqrt{K}l_q)\right]^2\sigma_{22}, \end{aligned} \tag{3}$$

where $l_{q,d}$ are the quad and drift lengths, respectively, and the quadrupole field gradient B' is parametrized by the focusing strength $K = 299.8B'\,(\text{T})/pc\,(\text{MeV})$. With Eq. (3), one takes into account the full thick lens matrix, instead of the more common thin-lens analysis in which the betatron phase advance inside the quad is neglected. Typical quad scan data and the corresponding thick lens analysis fit are shown in Fig. 13.

Figure 14 shows the observed emittance growth as a function of PWT linac rf phase. It can be seen that a sharp

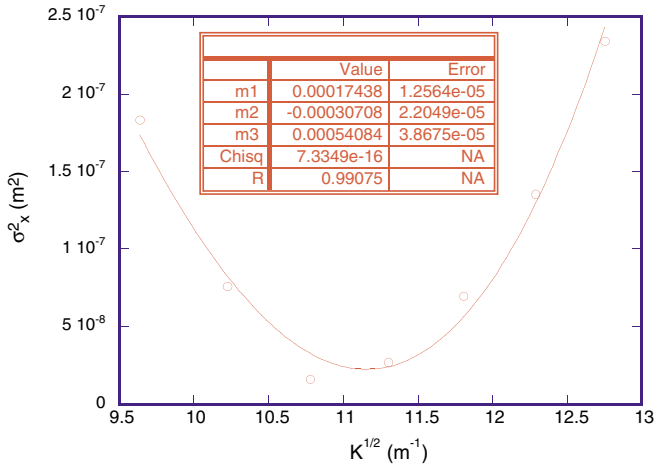

FIG. 13. (Color) Example data and fit for the thick lens quad scan of the central slice of a velocity-bunched beam. Here the mean square horizontal beam size is measured versus the focusing strength of the quadrupole, parametrized by $K = 299.8B'\,(\text{T})/pc\,(\text{MeV})$. The data is fitted to Eq. (3) (solid line) and the fit parameters are used to determine the rms emittance of the beam slice.

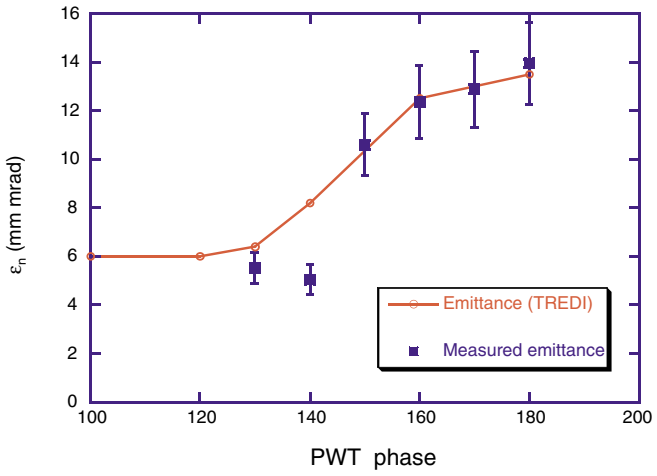

FIG. 14. (Color) Emittance growth during compression, experimental results from quadrupole scan, and TREDI multiparticle simulations of compression and measurement system.

increase occurs as the phase approaches, but does not yet reach, that which gives rise to optimum bunching. To quantify this effect, we have employed a more sophisticated tool that can model 3D multiparticle collective effects. The simulation code TREDI [27] is a self-consistent tracking code that employs a 3D Lienard-Wiechert field calculator. It is capable of giving detailed phase space information, and allows an understanding of this measurement system that has an unexpected systematic problem arising from space-charge effects in the bend. Note that the simulation results given in Fig. 14 match the experimental data for the emittance growth well. These results can also aid in deducing the precise mechanism of this growth.

VI. COMPRESSION OF A BEAM WITH A CHIRPED ENERGY SPECTRUM IN A BENDING MAGNET

We expected to observe emittance growth for PWT phases where the longitudinal waist of the beam occurs before the measurement screen due to the effects of a longitudinal crossover in the transverse phase space. On the other hand, the experimental and simulation results shown in Fig. 14 display an emittance increase even for phases for which the beam does not near full compression in the drift between the PWT and the dispersing dipole. To explain this, a deeper look into the dynamics of an energy-chirped beam traversing a bend magnet is required. This investigation is carried out using both a linear model for the beam configuration space evolution and the full six-dimensional phase space model from TREDI simulations.

For the vertical phase space, the bending magnet is a simple drift. However, examining the beam distribution in (x-s) configuration space, one may observe notable rearrangement of particle positions. These may lead to a strong enhancement of the local beam density if the beam is initially chirped in energy, with particles having higher energy located in the tail of the beam. Note that a bending magnet has a negative $R_{56} = \partial z_f/\partial(\delta p/p)_i$ (defocusing for such a chirp) so that this effect cannot be ascribed to standard notions of longitudinal compression; it is therefore anomalous. The size of the projections of the beam extent onto the curvilinear longitudinal axis s or onto the transverse dimension x and y do not diminish in the bend. On the other hand, when one examines the mechanism for density increase, and accompanying emittance growth, with greater care, it is found that the physical three-dimensional volume of the beam can indeed become smaller, go through a minimum, and finally increase again inside of a dipole magnet. This is a 3D configuration space effect that may be important when a strong negative chirp $[d(\delta p/p)/d\zeta < 0]$ is imparted upon the beam before it traverses a simple bending magnet.

The negative effects on the beam quality of this electron density increase are dramatic, in both experiment and simulation, especially at moderately relativistic energies where space-charge forces dominate the dynamics of the beam. A similar effect was observed in the Neptune magnetic compression experiment, where configuration space correlations associated with the evolution of beam in the final chicane bend magnet gave rise to large phase space distortions [6].

A simple way to understand the physics of this process is through a matrix analysis. Because the vertical phase space is uncoupled in the bending magnet, we need only to concentrate on the four-dimension phase space $(x, x', s, \delta p/p)$. Given the initial beam matrix Σ,

$$\Sigma = \begin{pmatrix} \sigma_{xx} & \sigma_{xx'} & \sigma_{xs} & \sigma_{x\delta} \\ \sigma_{x'x} & \sigma_{x'x'} & \sigma_{x's} & \sigma_{x'\delta} \\ \sigma_{sx} & \sigma_{sx'} & \sigma_{ss} & \sigma_{s\delta} \\ \sigma_{\delta x} & \sigma_{\delta x'} & \sigma_{\delta s} & \sigma_{\delta\delta} \end{pmatrix}, \tag{4}$$

where the elements σ_{ij} are the second moment of the beam phase space distributions (for example, $\sigma_{xx} = \langle x^2 \rangle$, $\sigma_{xx'} = \langle xx' \rangle$, etc.). This matrix evolves according to the transformation,

$$\Sigma_f = \mathbf{R} \cdot \Sigma_i \cdot \mathbf{R}^{\mathbf{T}}, \tag{5}$$

where the transport matrix $\mathbf{R}$ for a flat-field bending magnet is

$$\mathbf{R}(s) = \begin{pmatrix} 1 & s & 0 & -R \cdot (1 - \cos(\frac{s}{R})) \\ 0 & 1 & 0 & -\sin(\frac{s}{R}) \\ \frac{s}{R} & \frac{s^2}{2 \cdot R} & 1 & \frac{s}{\gamma^2} - s + R \cdot \sin(\frac{s}{R}) \\ 0 & 0 & 0 & 1 \end{pmatrix}. \tag{6}$$

Here s is the longitudinal coordinate along the beam path, R is the bending radius, and γ is the Lorentz factor of the design energy.

One can then calculate the configuration space volume taking into account possible correlations between x and the longitudinal coordinate s,

$$V = \sqrt{\sigma_{xx} \cdot \sigma_{ss} - \sigma_{xs}^2}\sqrt{\sigma_{yy}}. \tag{7}$$

The transverse emittance contribution ($\sigma_{xx'}, \sigma_{x'x'} \approx 0$) may be neglected because the rf nonlinearities make the longitudinal trace space contribution to the final volume dominant. We may also take the vertical rms beam size $\sqrt{\sigma_{yy}}$ to be roughly constant over the region of interest, $\sqrt{\sigma_{yy}} = \sqrt{\sigma_{yy,0}}$. With these assumption one obtains for the configuration space volume

$$V = \sqrt{\sigma_{xx}(\sigma_{ss} + 2\sigma_{s\delta}R_{56}^* + \sigma_{\delta\delta} \cdot R_{56}^{*2}) + R_{16}^2(\sigma_{ss}\sigma_{\delta\delta} - \sigma_{s\delta}^2)}\sqrt{\sigma_{yy,0}}, \tag{8}$$

where the modified longitudinal transport element R_{56}^* can be written as

$$R_{56}^* = \frac{s}{\gamma^2} + R \cdot \sin\left(\frac{s}{R}\right) - s \cdot \cos\left(\frac{s}{R}\right). \tag{9}$$

Equation (9) indicates that R_{56}^* (in contrast to the standard matrix element, R_{56}) is a positive quantity and that increases quickly with distance (in the ultrarelativistic case, $\sim s^3$), and R_{16} is the horizontal dispersion function, also increasing with distance. The initial rms beam configuration space volume is $\sqrt{\sigma_{xx,0}\sigma_{ss,0}\sigma_{yy,0}}$. If the beam initially has a negative energy-position chirp, $\sigma_{s\delta} < 0$, so that particles in the tail are more energetic than particles in the head, this correlation can be removed by the positive R_{56}^* at the anomalous compression, or *minimum volume* point. The linear evolution of the configuration space volume, as well as the apparent projected configuration space volume $\sqrt{\sigma_{xx}\sigma_{ss}\sigma_{yy,0}}$, is shown in Fig. 15.

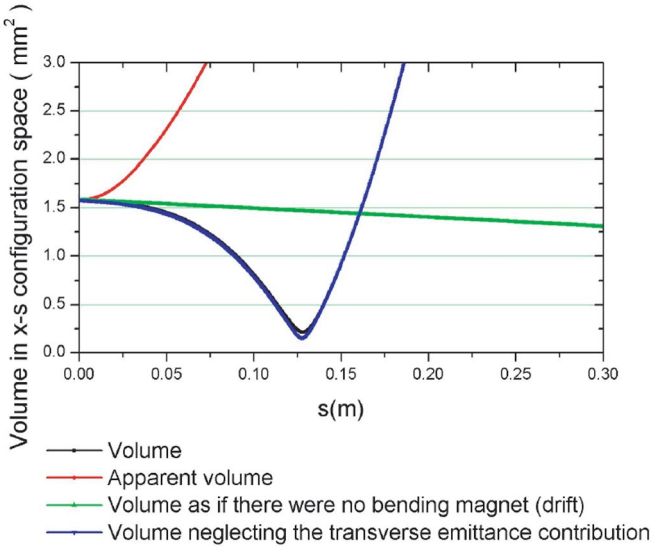

FIG. 15. (Color) Anomalous compression analysis for a beam chirped by traversing the PWT 70° off crest. The initial beam sizes at the entrance of the dipole magnetic field are $\sigma_x = 2.8$ mm, $\sigma_s = 0.6$ mm. Shown are the linear evolution of the configuration space volume, as well as the apparent projected configuration space volume $\sqrt{\sigma_{xx}\sigma_{ss}\sigma_{yy,0}}$. The anomalous compression point is 12 cm inside the magnet and the compression factor is 4.7.

The apparent projected volume was what drove our initial assumption that space-charge and related effects would be mitigated in the bend. Examining the projected volume, one may naively conclude that the beam becomes quickly more spread out in both x and s dimensions, thus lowering its density dramatically. This, as we have just demonstrated, is not always necessarily the case.

Geometrically the minimum volume conditions roughly corresponds to a point along the beam line in which the more energetic particles in the tail of the beam overtake the less energetic ones in the direction of initial beam motion z, as shown in Fig. 16.

The compression factor depends strongly on the initial transverse beam size and the longitudinal trace space emittance. It is given by

$$B = \frac{V_i}{V_f} = \sqrt{\frac{\sigma_{xx} \cdot \sigma_{ss}}{\varepsilon_s \cdot (\frac{\sigma_{xx}}{\sigma_{ss}}(R_{56}^*)^2 + (R_{16})^2)}}, \tag{10}$$

where ε_s is the longitudinal trace space emittance, and R_{16} and R_{56}^* are evaluated at the anomalous compression point.

The linear analysis is useful for obtaining a conceptual understanding of what happens to the beam distribution as it traverses the dipole bend. In order to fully understand our measurement we must, however, examine the 3D TREDI simulations. In doing so, we may observe not only the beam's density increase that occurs at the anomalous compression point, but also extract the growth of both $\varepsilon_{n,x}$ and $\varepsilon_{n,y}$ accompany this charge density. The success of the comparison of the TREDI model with the quadrupole scan results of Fig. 14 gives confidence that the TREDI results

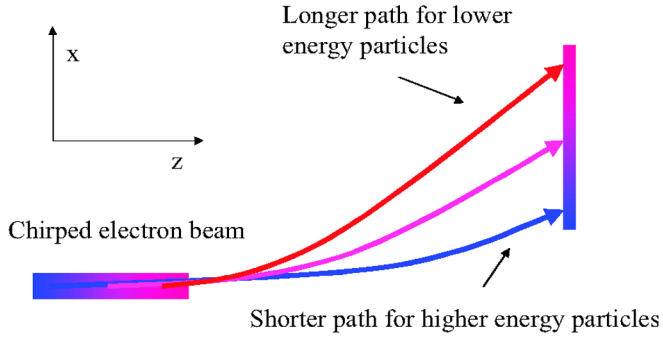

FIG. 16. (Color) Geometrical description of anomalous compression.

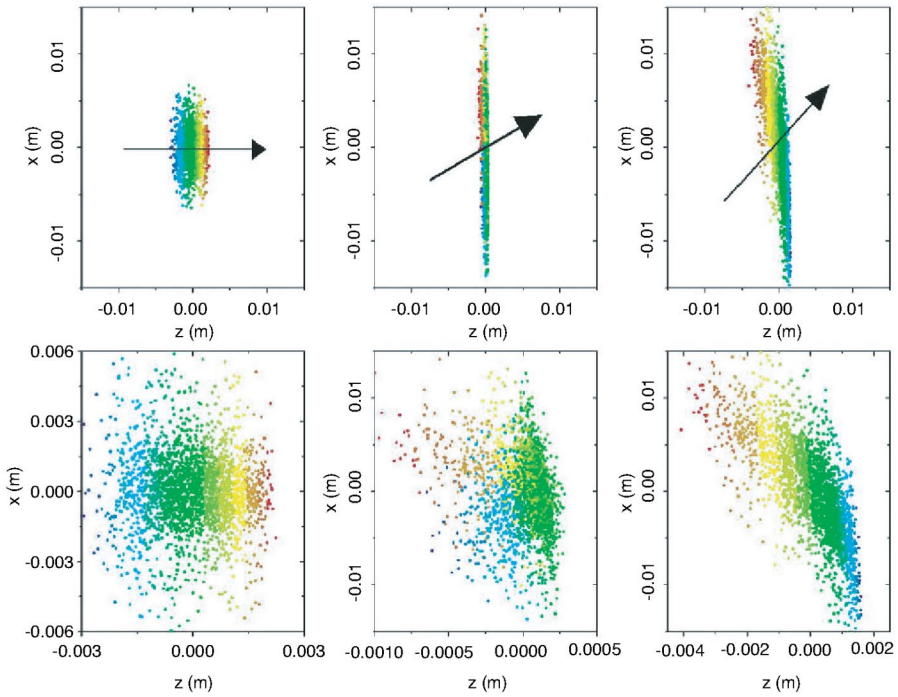

FIG. 17. (Color) Cartesian configuration space x-z projections for a beam accelerated 70° off crest in the PWT linac at three different locations along the Neptune beam line: before the dipole (first column), at the anomalous compression point 12 cm inside the dipole (second column), and after the crossover (third column). The top line has equal scale on x and z axes. An arrow shows the beam propagation direction. The bottom pictures are zoomed versions of the top ones with expanded axes. Particles with higher energy (blue) that were in the tail of the beam overcome the lower energy particles (red) in the front.

give insight into the microscopic mechanisms behind the observed emittance growth.

Examination of the configuration space in the TREDI simulations has shown that if the chirp on the beam is not too big ($< 10\%$ when the beam is accelerated 30° off crest), the crossover does not occur, because the dispersion (R_{16}) in the horizontal plane dilutes the beam before the anomalous compression point. In this case, the beam simply bends inside the dipole without strong degradation of phase space quality. On the other hand, for a beam with large energy chirp that has been accelerated far off crest in the bunching linac, a configuration space crossover (in z) takes place less than 10 cm after the entrance of the dipole, as is illustrated in Fig. 17. The more energetic particles initially in the tail reach the less energetic ones that follow a trajectory having a larger bending angle. The accompanying density increase is also easily seen in Fig. 17. This density increase is seen in the simulations to coincide in time with significant emittance growth; thus the density increase is indeed verified to be the reason for emittance growth even at phases for which the compression in the rectilinear drift is incomplete.

VII. CONCLUSIONS FROM NEPTUNE BALLISTIC BUNCHING MEASUREMENTS

The Neptune ballistic bunching experiments have illustrated both the physics involved in the ballistic bunching process and the limitations of the experimental techniques employed in the measurements. The measurement of the extent of the bunching represents a first test of the longitudinal dynamics of a thin-lens, ballistically bunched photoinjector beam. Our results show a notable improvement on those previously reported from both the velocity bunching measurements at BNL [14] and the magnetic compression results obtained at Neptune [6], despite the initial bunch length being longer in the present experiments.

In both cases, part of the improvement can be attributed to the use of the linear region of the rf wave near its zero crossing, with accompanying reduction of longitudinal emittance. Quantitatively, the Neptune experiments succeeded in lowering the observed σ_t from 0.6 ps in both Refs. [6,13] to less than 0.4 ps. This value raises the issue of the resolution of the CTR measurement. As we shall see, this question is more urgent in the LLNL velocity bunching measurements, where yet shorter bunches are observed. Discussion of σ_t measurement resolution and its potential improvement is thus delayed until the LLNL results are presented.

The measurement of transverse phase space in the Neptune experiments definitively shows emittance growth. This is an important, albeit expected result. On the other hand, the observed growth could not be fully attributed to space-charge effects due to rectilinear motion, but partially to a systematic collective effect in the measurement. This is

also not surprising, as there are many scenarios in high-brightness beam experimentation [28,29] where collective effects obscure the measurement being undertaken. In an effort to utilize the time correlation in the beam energy spread, we have adopted a beam-slicing technique. While it was initially predicted from the standard projection of the beam distribution onto the locally Cartesian design axes that bending effects would cause the beam to become less dense, the opposite was found to be true. Thus as a side effect of this investigation, a novel effect—anomalous density increase of energy-chirped beams in bends—has been brought to light.

While it is interesting to study the intermediate state of the beam as it undergoes velocity bunching, it has been far from straightforward to do so. In addition to collective effects, beams with such large energy spread found in the Neptune experiments are difficult to unambiguously diagnose. We thus proceed to study beams at LLNL that have been completely velocity bunched, with the bunching arrested, and the energy spread removed as well as possible. The experiments presented are performed in a different regime, that of phase space rotation in a long linac. The physics of bunch compression in this regime are discussed within the context of the experimental setup located at the LLNL ICS facility, PLEIADES. This facility allows not only the opportunity for optimized bunch compression and energy spread mitigation, but it also contains focusing solenoids that can be used to control the emittance growth that asserts itself during the compression.

VIII. VELOCITY BUNCHING USING PHASE SPACE ROTATION

Velocity bunching, in the form initially proposed by SF, differs from the ballistic bunching technique discussed above. While in ballistic compression the rf structure is used to impart a longitudinal phase space correlation that is removed later by a drift, in the phase space rotation method, the energy/phase correlation is imparted and removed smoothly, through phase slippage and acceleration, inside of the rf linac section. In this method the beam is rotated through one quarter of a phase space oscillation, as illustrated in Fig. 18.

To understand the velocity bunching mechanism in detail, we perform an analysis similar to that of SF, but using a speed-of-light phase velocity wave, as is available at the PLEIADES linac, instead of a slow-wave treatment. If one follows the arguments of SF, it can be seen that a speed-of-light phase velocity may give very close to optimum compression, as deduced from a phase space mapping analysis, which we will review below. The analysis of SF emphasizes the utility of slowing the wave phase velocity in the bunching system, in which case one may obtain a quarter-rotation of the phase space concomitant with acceleration of the beam. This idealized rotation begins with a beam having no initial phase-energy correlation, injected at the zero crossing of the wave, and ends with maximum energy spread and minimum phase extent.

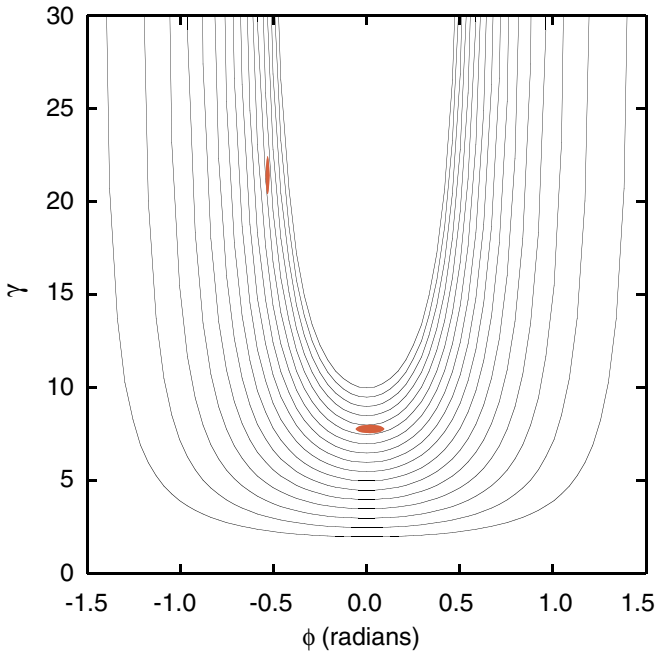

FIG. 18. (Color) Longitudinal phase space particle trajectories in a traveling wave linac section modeled by a sinusoidal accelerating field. The rf parameters used in the plot are typical values for the LLNL 100 MeV linac. The plot illustrates the phase space rotation compression mechanism for a bunch injected near the rf zero crossing.

In practice, the fact that this quarter-wave rotation from the ideal initial condition is not typically achieved in a speed-of-light accelerating wave is not critical, as one may simply choose a slightly different initial rf phase to provide further rotation. Also, the tuning of the phase velocity is used in the SF scheme to change the distance along the accelerator required to obtain a quarter synchrotron oscillation. This is helpful, as in the absence of such an option, one must rely on tuning of the accelerating field amplitude alone. In practice, this concern is also mitigated, since the linac sections at PLEIADES are relatively short (2.5 m), and adjustments in the phase between sections may be used to fine-tune the acceleration scheme, in a way that is functionally equivalent to changing the phase velocity. Because of these considerations, one may view the PLEIADES setup as essentially equal in effect to the ideal case analyzed by SF. As a final comment, we note that the minimum bunch length achievable in this system is dominated by the distortion of the final phase space by the nonlinearity of the sinusoidal forces used. This effect may be mitigated by use of higher harmonic rf cavities in addition to the fundamental.

We begin our analysis by considering the (averaged over the fast fluctuations of the field occurring in a single cell of the linac) interaction of an electron with the sinusoidal longitudinal electric field component of the rf wave in a

traveling wave structure,

$$E_z = E_0 \sin(\phi), \tag{11}$$

where $\phi = kz - \omega t + \phi_0$ is, as in our discussion of the ballistic buncher, the electron phase with respect to the wave, and $k = \omega/c$ for the speed-of-light wave. Our phase convention is such that peak acceleration occurs when $\phi = -\frac{\pi}{2}$. With this electric field, the electron motion obeys a time-independent Hamiltonian (which is thus a constant of the motion) of the form

$$H = \gamma - \sqrt{\gamma^2 - 1} - \alpha \cos(\phi), \tag{12}$$

where $\alpha \equiv eE_0/mc^2k$ is the dimensionless vector potential amplitude of the wave. The electron trajectories can be tracked and plotted in (ϕ, γ) phase space using the electron equations of motion:

$$\frac{d\gamma}{dz} = -\alpha k \sin\phi, \tag{13}$$

$$\frac{d\phi}{dz} = k\left[1 - \frac{\gamma}{\sqrt{\gamma^2 - 1}}\right]. \tag{14}$$

Examples of these phase space trajectories, which follow curves of constant Hamiltonian, are shown in Fig. 18. In this case, trajectories are plotted for typical rf parameters at the LLNL 100 MeV linac, $k = 59.8\ \mathrm{m}^{-1}$, $\alpha = 0.3$ and with a minimum γ between 2 and 10.

As the plot shows, particles injected at or near $\phi_0 = 0$ will begin to slip into an accelerating phase. As the particles accelerate to ultrarelativistic velocity, the phase slippage slows, and is eventually arrested. This can be seen by using $\gamma \gg 1$ in Eq. (14), giving $d\phi/dz \cong -k/2\gamma^2$, which tends to zero sufficiently quickly for ϕ to approach a finite asymptote. The asymptotic phase limit can be found from Eq. (12) to occur when $H = -\alpha\cos\phi$. In terms of the initial conditions ϕ_0 and γ_0, the phase as $\gamma \to \infty$ is

$$H = -\alpha\cos\phi_\infty = \gamma_0 - \sqrt{\gamma_0^2 - 1} - \alpha\cos\phi_0, \tag{15}$$

or

$$\phi_\infty \cong \cos^{-1}\left[\cos\phi_0 - \frac{1}{2\alpha\gamma_0}\right], \tag{16}$$

where, as above, the approximation $1 - \beta \cong 1/2\gamma^2$ has been used.

The phase space rotation occurs as a result of the varying orientation of the phase contour lines. If two particles are injected at $\phi_0 = 0$ with a difference in phase but no spread in energy, such that they align parallel to a phase contour, then they will remain parallel to that contour as they slip in phase and accelerate. As the particles approach ϕ_∞, their orientation becomes nearly parallel to the γ axis, having rotated by nearly 90°. To evaluate the phase compression that occurs for a beam with nonzero initial phase and energy spreads, $\Delta\phi_0$ and $\Delta\gamma_0$, respectively, one can assume for simplicity that the extraction phase is ϕ_∞. In that case, expanding Eq. (16) to first order in the initial energy spread and second order in the initial phase spread gives

$$\Delta\phi_\infty = \frac{\sin\phi_0}{\sin\phi_\infty}\Delta\phi_0 + \frac{1}{2\alpha\gamma_0^2\sin\phi_\infty}\Delta\gamma_0 + \frac{1}{2}\left[\frac{\cos\phi_0}{\sin\phi_\infty} - \frac{\cos\phi_\infty\sin^2\phi_0}{\sin^3\phi_\infty}\right](\Delta\phi_0)^2. \tag{17}$$

Using $\Delta\gamma_0/\gamma_0 = 10^{-3}$, $\Delta\phi_0 = 4°$, $\gamma_0 = 8$, $\alpha = 0.3$, and $\phi_0 = 0$ results in a final phase spread of $\Delta\phi_\infty = 0.2°$, and a compression ratio of roughly 20.

It is important to note that for this example, the $(\Delta\phi_0)^2$ term in Eq. (17) is an order of magnitude larger than the $\Delta\gamma_0$ term, thus explaining our dropping of the term proportional to $(\Delta\gamma_0)^2$. The fact that the phase spread of the injected beam limits the minimum final bunch length is a result of nonlinear rf forces increasing the longitudinal emittance of the beam. This can be understood by examining the constant Hamiltonian lines at the injection and

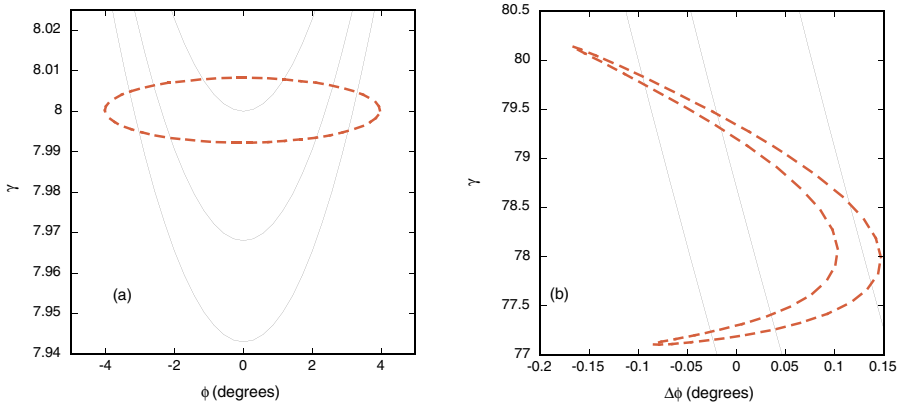

FIG. 19. (Color) (a) Phase contours (solid lines) intersecting an ellipse (dashed line) representing the injected beam distribution. (b) Phase contours (solid lines) and extracted beam phase space (dashed line) obtained by integrating Eqs. (13) and (14) for points on the injected beam ellipse.

extraction points. At $\phi_0 = 0$ the phase contours, $\gamma(\phi, H)$, have a curvature that does not follow the outline of the injected beam ellipse (using the same parameters as above). As the beam transforms under the influence of acceleration and slippage these contours "straighten out" near the asymptotic phase, forcing the initial ellipse to distort, gaining a nonlinear correlation and therefore, an increased emittance. This process is illustrated in Fig. 19, which shows the phase contours intersecting the initial beam ellipse in (a) and the same contours in (b) as the phase approaches ϕ_∞, with the resulting distorted beam shape.

IX. VELOCITY BUNCHING AT PLEIADES

The PLEIADES facility at LLNL produces picosecond pulses of hard x rays (10–200 keV) by colliding an ultrarelativistic electron beam (20–100 MeV) with a high intensity, 50 fs, 800 nm laser pulse. This x-ray source is designed to enable pump-probe experiments used to temporally resolve material structural dynamics on atomic time scales [4]. The PLEIADES project follows the results of previous ICS generation of subps pulses of hard x rays, demonstrated at the LBNL Advanced Light Source injector linac, with (30 keV) x-ray beam fluxes of 10^5 photons/pulse [30,31]. In addition, ICS x rays have notably been created at the Naval Research Laboratory [32] and the ATF [33], and in the γ-ray spectral region at KEK [34].

The duration of the x-ray pulse generated though this scattering process is determined by the duration of the overlap of the electron and laser beams. Thus, to produce subpicosecond x-ray pulses desirable for pump-probe experiments, one may choose a 90° interaction geometry, in which the laser samples only part of the highly focused electron beam, or a 180° geometry, where the laser interacts with the entire electron bunch, which must be compressed to subpicosecond length.

Bunch compression is therefore an attractive option for the facility, but since the brightness of the x-ray source depends critically on the electron beam spot size ($B \propto \sigma^{-4}$), the bunching method used must be evaluated to determine if negative effects on the emittance or energy spread of the beam will reduce x-ray brightness to an unacceptable level. Velocity bunching is an obvious choice for this application, because the compression effectively occurs at low (gun exit) energy, and thus one may remove much of the energy spread that can cause unacceptable chromatic aberrations in the ICS final focus. The PLEIADES experiments thus also afford us the ability to examine effect of velocity bunching on the ICS source.

The PLEIADES photoinjector and linac consist of a 1.6 cell photocathode rf gun followed by four SLAC style 2.5 m, *S*-band traveling wave sections. While the linac is capable of producing 100 MeV electrons, it is typically run using only the first two or three sections for x-ray production, resulting in beam energy between 20 and 70 MeV. The gun and each linac section are powered by separate klystrons, making power and phase control independent for each accelerator section. We simulated the velocity bunching process in this system using HOMDYN and PARMELA, as in the ORION study above. In this case, however, experimental values of the accelerating gradients in the different accelerators were used in the simulations.

In Fig. 20 the pulse length and relative momentum spread evolution are simulated using HOMDYN. The gun field gradient used in this simulation was 75 MV/m (limited by rf breakdown at the time of the measurements) and the charge was 0.25 nC. As the figure shows, these parameters result in significant bunch lengthening and increased energy spread after the gun. At the entrance to the compressor section, the beam correlation in longitudinal phase space is the opposite of that required for compression. It is clear from the evolution of the energy spread in Fig. 20 that this correlation is quickly reversed in the compressor, but the presence of this correlation requires a larger amount of phase space rotation in order to fully compress the beam. Consequently, it was found in these simulations that the injection phase that gives the shortest output bunches was 17° (i.e., ahead of the zero crossing). It is interesting to note that the optimal injection phase even for an idealized, uncorrelated beam was found to be about 2° forward of zero crossing. This is because the average exit phase of the

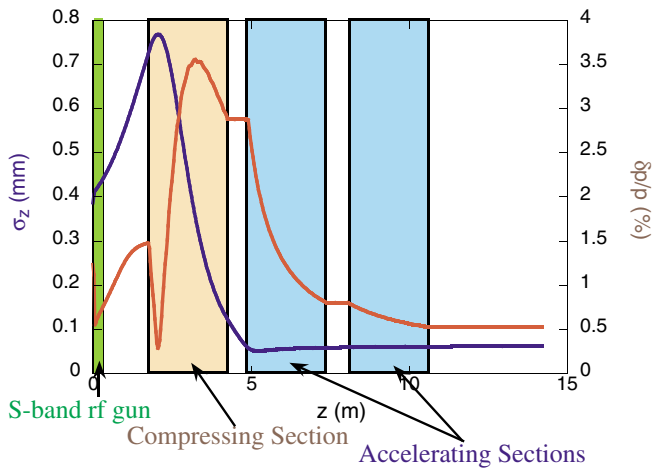

FIG. 20. (Color) HOMDYN simulation of the bunch length and relative energy spread in the velocity-bunching scheme implemented at PLEIADES. The bunch charge in this case is 250 pC. The rms bunch length (plotted in blue) initially increases in the drift region between the rf gun and the compressing traveling wave linac section. Unlike the ORION simulations, the majority of the compression occurs within the first linac section and the minimum bunch length, 50 μm, is achieved at the entrance to the second linac section. The rms energy spread (plotted in red) follows a pattern similar to the ORION case, peaking at a few percent in the compressor and decreasing in the following two sections to a final value of 0.5%.

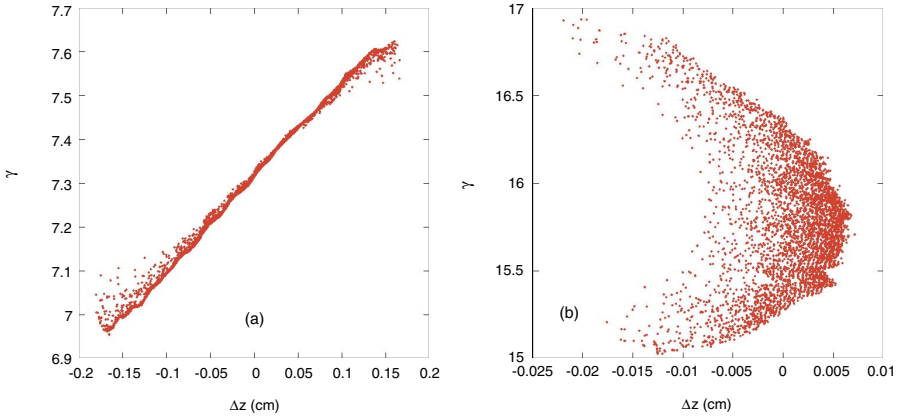

FIG. 21. (Color) PARMELA simulation of the longitudinal phase space (a) before the compressing rf section and (b) after the section. A clear debunching correlation is present and must be removed at the beginning of the bunching section.

beam is not ϕ_∞, since the rf section has a finite length. The phase contours at the beam exit point have a finite slope, and injecting slightly ahead of $\phi = 0$ compensates for this slope.

Figure 21 shows the longitudinal phase space plots in PARMELA simulations for the injected and extracted electron bunches. The strong debunching phase space correlation of the injected beam is clearly evident. The simulated rms bunch duration reaches a minimum value of approximately 200 fs, and does not change significantly after the compressor. The rms relative energy spread at the end of the compressing section is 3%. In the two accelerator sections after the compressor, the beam is injected at $\phi = -\pi/2$ for maximum acceleration. Immediate acceleration of the beam is important, as it arrests the bunching process, decreases the relative energy spread, and mitigates the extremely strong transverse space-charge forces on the bunch, which at this point has 500 A peak current and low energy ($\gamma = 16$).

The final beam energy predicted by simulation was 50 MeV. The final rms energy spread, as shown in Fig. 20 is 0.5%. The energy spread produced by simulating all three sections on crest is 0.2%, in agreement with beam measurements. This increase in energy spread is potentially problematic, since it can limit the minimum spot size achievable in ICS x-ray generation. It was found, however, that emittance is the dominant factor for our experiments so that emittance growth and not energy spread is the larger concern for x-ray production.

As was done in the ORION simulations, control of the transverse dynamics is accomplished with the solenoids that are placed around each of the traveling wave sections. Emittance growth is avoided by choosing the focusing strength of the solenoids to match the defocusing space-charge forces on the beam. This process is illustrated in Fig. 22, which shows the evolution of the horizontal spot size and normalized emittance of the beam as it compresses. The gun solenoid strength is set to match the beam into the compressor section in the manner prescribed by emittance compensation. From the compressing section the solenoid strengths are set to minimize beam size oscillations through the system. The emittance oscillations, as in the ORION simulations, increase in frequency as the bunch compresses and subsequently slow as the beam accelerates. This is a sensitive process; the plot in Fig. 22(b) shows emittance

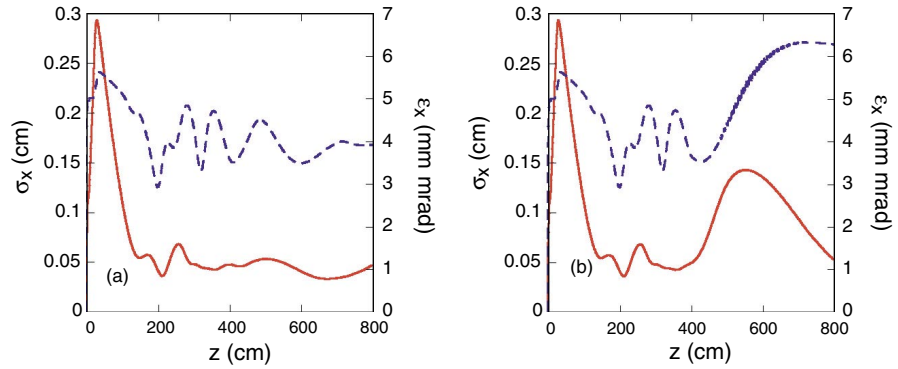

FIG. 22. (Color) PARMELA simulation of the rms spot size (solid line) and normalized emittance (dashed line). In (a) the solenoid strengths are chosen to keep the beam size constant in the compressing and accelerating sections. The beam is mismatched in (b), resulting in emittance growth.

growth caused by mismatching one of the section solenoids.

In addition to this matching sensitivity, it was also observed in the simulations that emittance growth was a very sensitive function of compression. When the beam compresses to the point of longitudinal phase space wave breaking, the emittance compensation (or more aptly, control of oscillation) process no longer works well.

X. PLEIADES BEAM MEASUREMENTS

The phase space rotation method has been used in the PLEIADES system as described in the previous section. The beam and accelerator parameters were measured and used to generate the simulations shown above. Specifically, a 250 pC, 3.5 MeV bunch was generated with the 1.6 cell gun and compressed in the first of three traveling wave sections used in the experiment. The accelerating gradients of the first to last sections were 5, 10, and 10 MeV/m, respectively, with the low gradient in the first section due to low available klystron power.

As in the Neptune measurements, CTR interferometry was used to measure the subpicosecond pulses we produced. The experimental procedure used to compress the beam was complicated by the significant variation of the phase slippage in the compressor section with injection phase. As a result, it is insufficient to change only the phase of the initial linac (compressor) section and ignore the phases of the following sections. A calculation of the dependence of phase slippage on injection phase is shown in Fig. 23; it indicates that the amount of phase slippage increase from the best acceleration phase to the best compression phase is more than 30°. Phasing the following sections appropriately must be done to properly accelerate on crest, thereby arresting the phase space rotation and minimizing the relative energy spread.

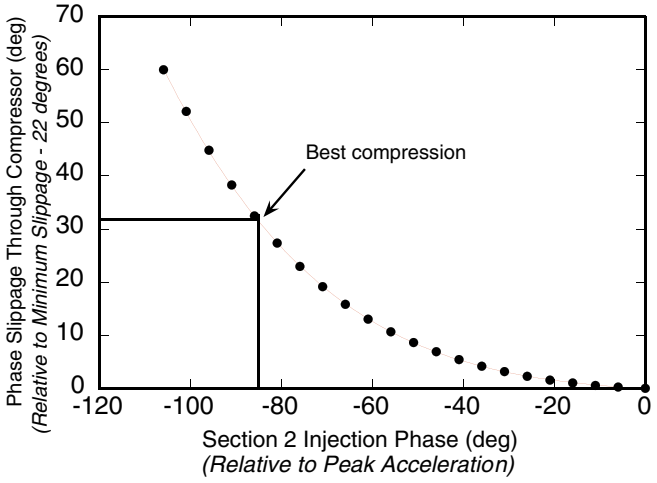

FIG. 23. (Color) Model calculation of the phase slippage in the compressor as a function of injection phase. The injected phase is relative to the phase for best acceleration, 20° ahead of crest.

The electron bunch was compressed by initially tuning the linac for highest energy. The phase of the compressor section was then set and the phases of the accelerating sections were also set using the calculation in Fig. 23 and fine-tuned by maximizing the CTR detector signal. The interferometer data obtained for the shortest bunch length achieved is given in Fig. 24. The data analysis was performed using the same method as with the Neptune case; the fit gives a 300 fs rms minimum σ_t. The interferometer wire spacing issues are identical to those discussed for Neptune, and they indicate that problems are expected for σ_t of 300 fs or below. The present measurement therefore gives an upper bound to σ_t, which is a bit longer than given in simulations ($\sim$ 200 fs), as seen in Fig. 20. Note also that this measurement produced even shorter beams than the Neptune case at the same charge. This is most importantly due to the shorter initial pulse length (2.5 ps rms) in the PLEIADES case.

The compressor phase for strongest compression was measured at 85° ahead of the best acceleration phase, which, because of the amount of slippage through the section, is not at, but about 20° ahead of, crest. This agrees well with simulations. The energy spread was measured at the linac exit using a spectrometer magnet, and found to be roughly 0.5%, as shown in Fig. 25.

For both the compressed and uncompressed electron beams, the emittance was measured using quadrupole scanning. The best emittance achieved in the uncompressed case was considerably poorer than that predicted by PARMELA. This is most likely due to poor spatial profile of the photoinjector drive laser, observed misalignments of the section solenoids, and coupling between the x and y phase planes. The emittance was observed to be asymmetric in x and y, with best values obtained $\varepsilon_{n,x} = 5$ mm mrad and $\varepsilon_{n,y} = 12$ mm mrad. These problems make the study of emittance of the compressed beam somewhat difficult to interpret.

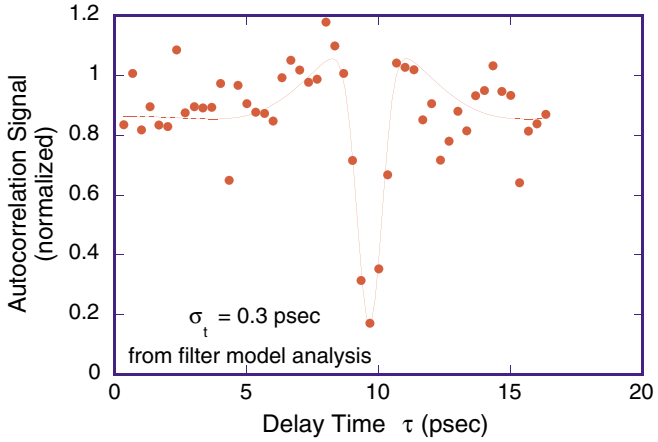

FIG. 24. (Color) Autocorrelation data for the optimally compressed bunch at PLEIADES.

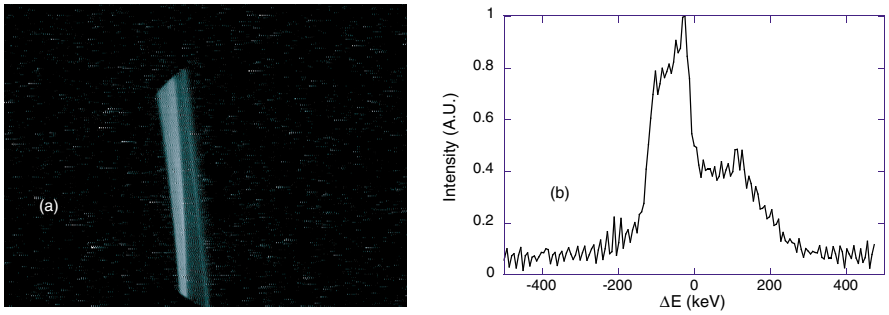

FIG. 25. (Color) (a) Image of the compressed beam at the spectrometer. (b) Lineout of the image in (a). The relative, rms energy spread is roughly 0.5%.

Nonetheless, from simulation and emittance compensation theory, we expect the emittance of the output beam to be a strong function of the focusing applied in the compressing section. Quad scan data taken with the fully compressed beam, varying the current in the first linac solenoid, is shown in Fig. 26. As expected, the emittance shows a very strong dependence on the compressor focusing, growing by a factor of 3 in $\varepsilon_{n,x}$ with a 20% change in solenoid current. A minimum of 11 mm mrad in both emittances was found to occur at the 10 A solenoid setting in this scan.

The asymmetry in the emittance of the beam results from focusing an asymmetric beam with a solenoid magnet. The initial asymmetry may be caused by an out-of-round laser spot on the photocathode, or unwanted normal and skew quadrupole fields in the gun or elsewhere. The solenoidal mixing of the coordinates x, y, x', y' of the beam particles give rise to phase space correlations in (x, y), (x, y'), and (x', y), as pointed out by Hernandez [35]. The mixing implies that $\varepsilon_{n,x}$ and $\varepsilon_{n,y}$ are no longer constants of the motion, but depending on both the amount of rotation applied by the solenoid magnets and the particulars of the downstream optics. In fact, because these "mixed" correlations are nonzero, the 4D phase space area is no longer given by the product $\varepsilon_{n,x}\varepsilon_{n,y}$ but by the determinant of the full 4D σ matrix; $\varepsilon_{4D} = \det|\sigma|$, where the matrix element σ_{ij} is given by $\sigma_{ij} = \frac{1}{N_e}\int x_i x_j f(\mathbf{x}, \mathbf{x}') d^2\mathbf{x} d^2\mathbf{x}'$.

This effect on the emittance can be seen in the beam (either compressed or uncompressed) by observing the (x, y) correlation, that is, by measuring σ_{13}. Figure 27 shows a typical beam at the end of the linac, in which a strong (x, y) correlation is evident. Considering this effect, a proper comparison of the compressed and uncompressed

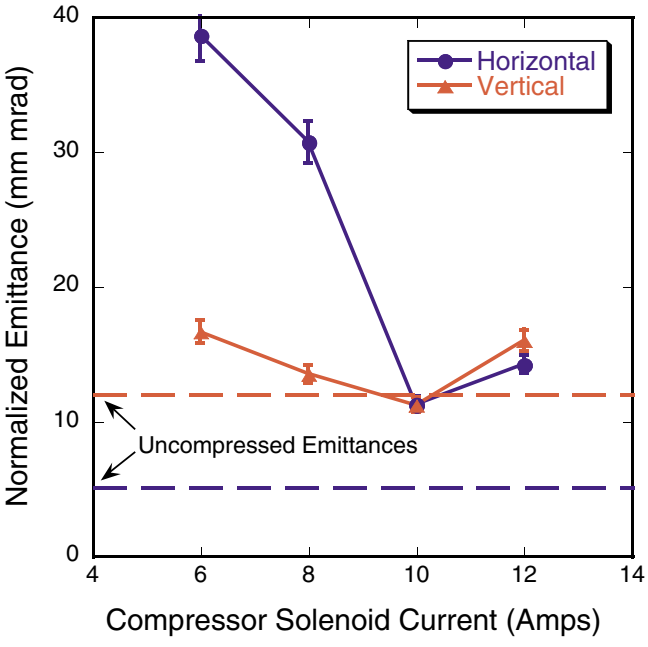

FIG. 26. (Color) Measured horizontal and vertical normalized emittances of the 300 fs beam versus the compressor solenoid strength.

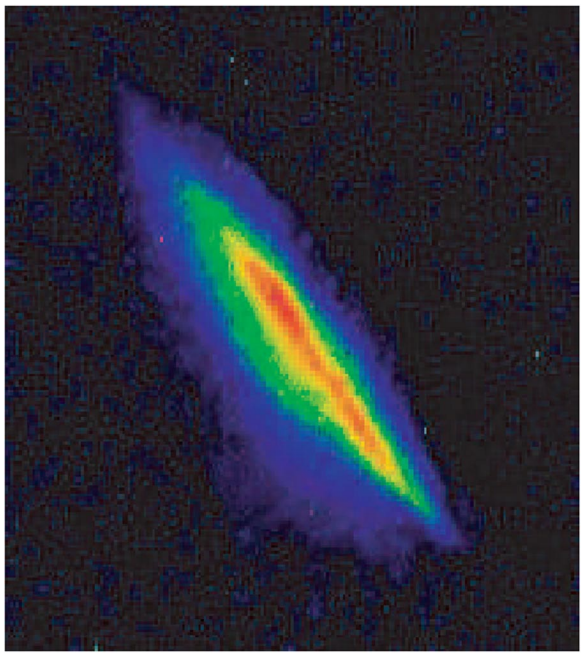

FIG. 27. (Color) False-color image of the electron beam showing a strong x-y correlation.

beams must examine ε_{4D}. This type of analysis follows that of Ref. [35], and is currently under development at PLEIADES. It is clear, however, based on focusability considerations in the ICS experiments, as described below, that non-negligible emittance growth occurs for the compressed beam.

XI. ICS X-RAY GENERATION WITH VELOCITY BUNCHED BEAMS AT PLEIADES

While compression of electron beam to ultrashort length using velocity bunching, well shorter than in Ref. [14], is of high interest, application of this beam is perhaps more compelling. The compressed electron bunch was used in ICS experiments to generate subpicosecond, 78 keV x rays at PLEIADES. A schematic of the experiment is given in Fig. 28.

The electron beam line consists of two quadrupole triplets, the first used to measure the beam Twiss parameters at linac exit, and to match into the second set, which serve as the final focus optics before the laser-electron interaction. In addition, there are pop-in diagnostic cubes, one used to generate CTR for the bunch length diagnostic and the other to transversely image the beam. The femtosecond accelerator laser concept (FALCON) Ti:sapphire-based laser system delivers a 500 mJ, 50 fs (FWHM) pulse of 800 nm light to the interaction area. The laser is focused by a 1.5 m focal length off-axis parabolic lens, and directed by a final turning mirror into the 180° interaction geometry shown in Fig. 28. The x rays generated at the interaction point propagate in the direction of the electron beam, pass through the final mirror, and are detected by a CsI scintillator fiber coupled to a 16-bit charge-coupled device (CCD) camera.

Two of the technical requirements of the ICS experiment are the ability to overlap the two beams spatially and temporally at the interaction point and to achieve the highest beam densities possible at that point. These issues are addressed with a diagnostic inserted at the interaction point. A 0.76 cm, polished aluminum cube, mounted on a three-axis translation stage, is placed in the beam path as illustrated in Fig. 29.

In one position the cube reflects the (highly attenuated for measurement purposes) laser and the optical transition radiation (OTR), generated by the electron beam passing

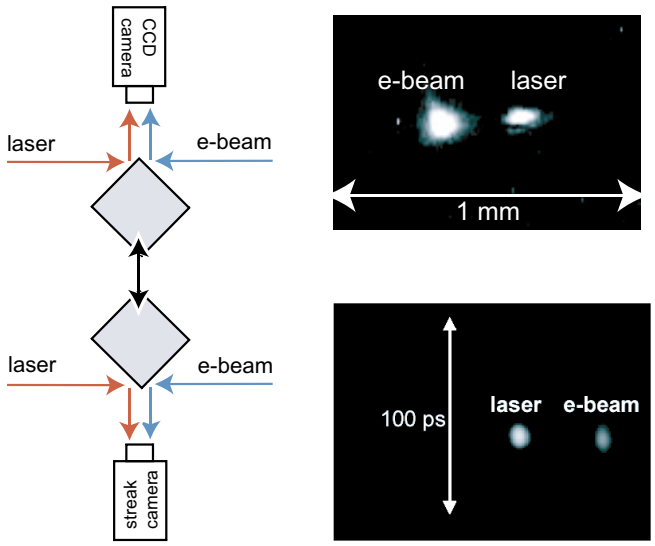

FIG. 29. (Color) Illustration of the interaction point diagnostic. In one position (top) both the laser and OTR light are directed to a CCD video camera. By moving the cube transverse to the beam path (bottom), the light is redirected to a streak camera.

through the cube surface, out of the vacuum chamber to a CCD video camera. When the cube is translated horizontally, the beams hit adjacent sides of the cube, and the light signals generated are redirected out the opposite vacuum port to a streak camera.

Typical optimized focused electron beam spots at the interaction point are shown for both the uncompressed and compressed cases in Fig. 30.

The bunch charge in both cases was 250 pC. The compressed beam was measured to be roughly 50% larger in x and y than the uncompressed beam. The rms dimensions of both beams are given in Table I.

Temporal overlap was accomplished by streaking the two beams at the interaction point. Streaking also allowed us to examine the timing jitter and drift of the beams. Picosecond level timing jitter is obtained at PLEIADES by using a single laser oscillator as the source that seeds both the ICS laser and the photocathode drive laser. The low level rf is also generated by frequency multiplying a photodiode signal from the same laser oscillator. With the rf and laser pulses synchronized in this way, the timing

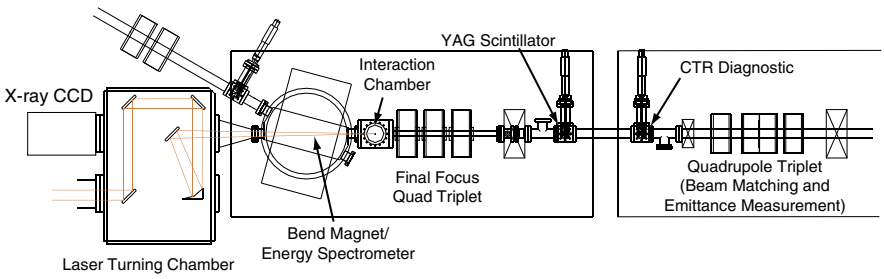

FIG. 28. (Color) Schematic layout of the PLEIADES ICS x-ray source experiment.

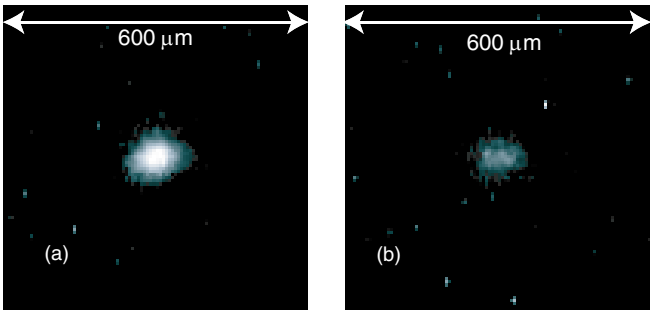

FIG. 30. (Color) CCD images of the (a) uncompressed and (b) compressed electron beam spots at the interaction point.

jitter at the interaction point has been measured to be 2 ps rms, which is at the resolution limit of the streak camera employed.

The process of bunch compression suppresses differences in injection phase, as measured with respect to the rf clock [36], demagnifying the initial laser-to-rf jitter by approximately the compression ratio. Thus because the FALCON and photoinjector drive laser are nominally locked, the tendency of the photoelectron beam to be locked to the rf clock by compression should increase the electron beam/FALCON laser jitter. The compressed bunch was streaked at the interaction point in order to measure this effect. An analysis of three different sets of streak camera images, each set taken a few minutes apart, was performed and the result is shown in Fig. 31.

The shot-to-shot jitter was found to be 2–4 ps rms, which was slightly higher than that obtained with the uncompressed beam. More impressively, the laser and electron beam timing drifted noticeably over time, an effect not seen with uncompressed electrons. This drift was observed to be as large as 35 ps, and occurred on a time scale of several minutes. The phase of the gun and each of the TW sections in the linac are measured and feedback loops are in place to prevent phase drift on a time scale longer than a second. The observed time-of-flight drift may be due to slow drifts in the klystron power output feeding the compressor section, which is not controlled by a feedback loop. This drift affects x-ray production in the uncompressed case as well, since it alters the beam energy, thereby affecting the steering and focusing of the electrons at the interaction point.

To produce x rays, the energy of the compressed electron beam was increased to 58 MeV by increasing the amount

TABLE I. rms sizes of the compressed and uncompressed electron beams at the interaction point.

Dimension	Compressed beam	Uncompressed beam
x	50 μm	30 μm
y	35 μm	25 μm
z	0.1 mm	1.0 mm

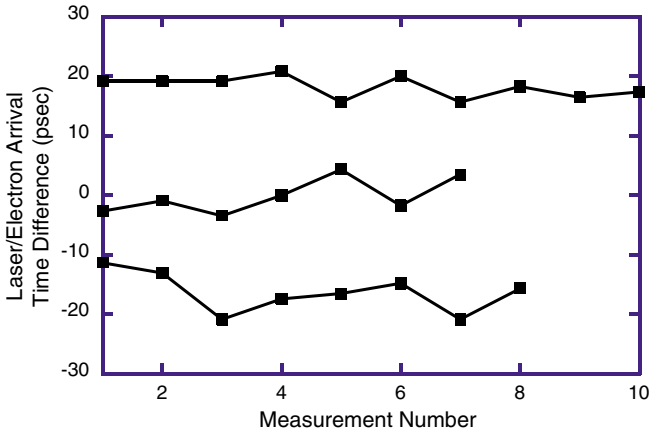

FIG. 31. (Color) Laser to electron beam timing jitter measurements taken at three different times. The shot-to-shot jitter is 2–4 ps while the total drift from the two extreme data sets is 35 ps.

of rf power in the final TW section. This was done to match the energy obtained under normal conditions, and therefore produce the same x-ray wavelength. Doing this makes the comparison of x-ray data simpler since it removes the energy dependence of the laser turning mirror attenuation and the calibration of the x-ray CCD (see Fig. 28). The bunch length and emittance dynamics are not affected significantly by increasing the energy in this way.

The ICS x rays were measured with the x-ray CCD camera for both the compressed and uncompressed beams. Figure 32 shows single shot x-ray beam data in these two cases.

The number of x-ray photons can be derived from the CCD images, and in the uncompressed case this number is $5 \times 10^6 \gamma$/pulse. For the compressed beam, a factor of 4–5 fewer photons were observed, yielding approximately $10^6 \gamma$/pulse. When the CCD camera is integrated over many shots the ratio of normal-to-compressed x rays increases. This is most likely a result of the timing drift discussed above.

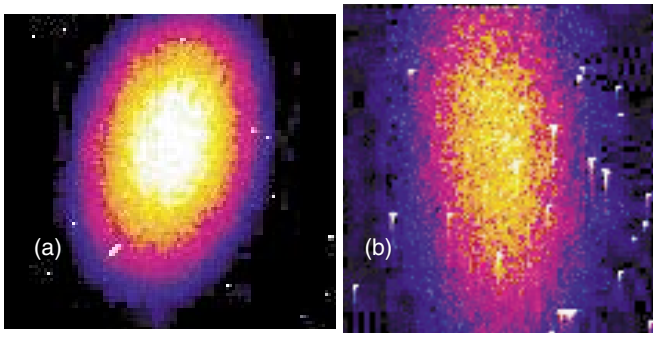

FIG. 32. (Color) Single shot, false-color x-ray beam images measured by the CCD for the (a) uncompressed and (b) compressed electron beams. The color scale has yellow as most intense, with violet as lowest non-negligible intensity observed.

The degradation of x-ray photon yield with velocity-bunched beam is due to the loss of electron beam focusability, which arises because of both emittance growth and final focus chromatic aberrations that increase in importance with the enhanced energy spread of a velocity-bunched beam. At the present time, the electron beam final focus has been upgraded to an extremely short focal length, permanent-magnet quadrupole (PMQ)-based system [37]. This improvement allows the mitigation of chromatic aberrations while lowering the minimum β function at focus, thus giving the potential to obtain much smaller spots. Much smaller spot sizes have been obtained with this system, but not as yet with velocity bunching deployed.

XII. CONCLUSIONS

We have presented here two scenarios for velocity bunching, one employing ballistic bunching, and the other based on phase space rotation. The ballistic bunching scenario, which has not yet been discussed in the literature, was introduced in the context of the ORION injector. The physical issues surrounding its use were discussed using illustrative simulations. These simulations included the envelope code HOMDYN, which was used to identify the overall experimental parameters, and macroscopic envelope performance. In order to understand microscopic issues such as emittance evolution, it was necessary to use multiparticle simulations. It was shown that the bunch may be shortened by an order of magnitude in length using a short, high gradient linac section, followed by a drift to compress the beam. The compression is arrested in post-acceleration, longer linacs, which are embedded in magnetic solenoids with a tailored, increasing profile in z. These solenoids provide transverse focusing that serves to control the emittance oscillations that arise from the raising of the beam current during compression. This control is predicted to work well provided that a longitudinal ''crossover'' is avoided, a scenario already known to give emittance growth from low-energy chicane compression experiments.

Experimental investigations of the ballistic bunching scheme, carried out at the UCLA Neptune Laboratory photoinjector, allowed examination of the bunching stage of the scheme, but not postacceleration or emittance control. Excellent bunching performance, with over an order of magnitude compression factor, has been observed. This bunching effectiveness exceeded those seen in both Neptune chicane compression and BNL velocity bunching experiments. In addition, measurement of the transverse emittance growth as a function of bunching was attempted. The interpretation of these slice experiments was obscured somewhat by the presence of a previously unknown anomalous compression occurring in the dispersive dipole. This effect leads, according to three-dimensional Lienard-Wiechert code simulations, to emittance growth in addition to that occurring during the rectilinear propagation of the beam.

The concept of phase space rotation-based velocity bunching has been discussed here in the context of the PLEIADES injector, which is employed in ICS experiments at LLNL. This system is similar to the original proposal of SF, with the exception of the use of speed-of-light phase velocity. It was shown, through Hamiltonian analysis and HOMDYN simulations, that the slow-wave linacs emphasized by SF are not critically necessary, especially for the relatively short (2.5 m) low gradient linac sections. The PLEIADES injector system is outfitted with independently powered solenoids, allowing emittance control, which was shown to be both imperfect in effectiveness and sensitive to envelope injection mismatch. The multiparticle PARMELA simulations we employed have shown that the emittance control is nonetheless manageable until one compresses to the onset of longitudinal crossover effects.

In experiments at PLEIADES, an even shorter rms pulse length, $\sigma_t = 0.3$ ps, was achieved than that found at Neptune, and a factor of 2 shorter than that observed in a similar scenario at BNL SDL [14]. The PLEIADES measurement is near the minimum resolvable pulse length of the CTR interferometer used, and is thus consistent with the predictions of simulation and instrument resolution. Achieving this pulse length is accompanied by moderate emittance growth, which, along with chromatic aberrations, produce an increase in final spot size. Emittance control dependent on a focusing solenoid surrounding the compressor accelerating section, a critical component of the SF scheme, was demonstrated for the first time.

Based on these techniques, we have unequivocally shown the utility of the velocity bunching process for producing a decrease in x-ray pulse length, and an increase in photon brightness from the PLEIADES ICS. This spot size increase causes the yield to decline by a factor of 4, while the peak current rises by over a factor of 10. To put the overall performance of the PLEIADES experiment in perspective, the peak photon flux from the BNL ATF ICS experiment was measured to be 2.2×10^{18}/s (with 8×10^{18}/s to be deduced from experimental efficiency estimates); after compression, PLEIADES produces 1.4×10^{18} photons/s. We note that the ATF result was obtained partially by use of a very large number of incident laser photons; the PLEIADES result is based upon obtaining peak electron current, 340 A, as opposed to 140 A at the ATF experiments.

The performance of the PLEIADES system was limited by poor initial emittance in the beam after the gun, x-y coupling, by misalignment of the focusing solenoids, and by drifts in the rf system. Efforts are underway to improve all of these experimental characteristics, in order to achieve velocity-bunched beam spots as small as 10 μm rms using the new PMQ final focus system. The short focal lengths of the PMQ final focus allows the mitigation of chromatic

aberrations which also afflicted the present PLEIADES experiments.

One of the most compelling improvements in velocity bunching experiments would be to run the rf gun at much higher gradient, in order to improve the emittance performance, and move to higher beam charge cases. Such a system, the SPARC photoinjector [38], is now under construction in Frascati. The SPARC experiment, which is intended to demonstrate beam brightness that is consistent with driving of a very short wavelength FEL, will devote much of its agenda to optimized velocity bunching studies, with precisely aligned solenoids, slow-wave bunching linacs, and an array of advanced beam diagnostics. The bunch length diagnostics will include a new, higher resolution CTR interferometer based on amplitude splitting, not polarization [39], as well as an rf deflector which should provide sub-100 μm resolution. Additionally, plans are underway to install a fourth harmonic rf cavity, allowing a much more linear compression, and shorter bunch final lengths. The SPARC experiment promises to provide more definitive tests of the usefulness of velocity bunching for high-brightness electron beam production.

ACKNOWLEDGMENTS

The authors thank Luca Serafini for insightful discussions, and William Patterson, Gerry Anderson, and Shawn Betts for their contributions to the LLNL experiments. This work is supported by U.S. Department of Energy Grant No. DE-FG03-92ER40693. This work was performed under the auspices of the U.S. Department of Energy by the University of California, Lawrence Livermore National Laboratory under Contract No. W-7405-ENG-48, through ILSA Grant No. LS04-001-B, and the UC Campus Laboratory Exchange program.

[1] Stanford Linear Accelerator Center, Technical Report No. SLAC-R-0521, 1998.
[2] J. B. Rosenzweig, N. Barov, and E. Colby, IEEE Trans. Plasma Sci. **24**, 409 (1996).
[3] C. E. Clayton and L. Serafini, IEEE Trans. Plasma Sci. **24**, 400 (1996).
[4] S. G. Anderson *et al.*, Appl. Phys. B **78**, 891 (2004).
[5] H. Braun, F. Chautard, R. Corsini, T. O. Raubenheimer, and P. Tenenbaum, Phys. Rev. Lett. **84**, 658 (2000).
[6] S. G. Anderson, J. B. Rosenzweig, P. Musumeci, and M. C. Thompson, Phys. Rev. Lett. **91**, 074803 (2003).
[7] J. S. Nodvick and D. S. Saxon, Phys. Rev. **96**, 180 (1954).
[8] K. Ishi *et al.*, Phys. Rev. A **43**, 5597 (1991).
[9] S. Heifets, G. Stupakov, and S. Krinsky, Phys. Rev. ST Accel. Beams **5**, 064401 (2002).
[10] S. Reiche and J. B. Rosenzweig, Phys. Rev. ST Accel. Beams **6**, 040702 (2003).
[11] L. Serafini and M. Ferrario, in *Physics of, and Science with, the X-Ray Free-Electron Laser*, edited by S. Chattopadhyay, M. Cornacchia, I. Lindau, and C. Pellegrini, AIP Conf. Proc. No. 581 (AIP, New York, 2001).
[12] X. J. Wang, X. Qiu, and I. Ben-Zvi, Phys. Rev. E **54**, R3121 (1996).
[13] X. J. Wang, in *Proceedings of the 1999 Particle Accelerator Conference, New York* (IEEE, Piscataway, NJ, 1999), p. 229.
[14] P. Piot, L. Carr, W. S. Graves, and H. Loos, Phys. Rev. ST Accel. Beams **6**, 033503 (2003).
[15] Stanford Linear Accelerator Center, ORION Technical Report, 2002, http://www-project.slac. stanford.edu/orion/
[16] M. Ferrario, J. E. Clendenin, D. T. Palmer, J. B. Rosenzweig, and L. Serafini, in *Proceedings of the ICFA Advanced Accelerator Workshop on the Physics of High Brightness Beams, Los Angeles, 1999*, edited by J. B. Rosenzweig and L. Serafini (World Scientific, Singapore, 2000), p. 534.
[17] L. Serafini and J. B. Rosenzweig, Phys. Rev. E **55**, 7565 (1997).
[18] J. B. Rosenzweig *et al.*, Nucl. Instrum. Methods Phys. Res., Sect. A **410**, 437 (1998).
[19] S. G. Anderson and J. B. Rosenzweig, Phys. Rev. ST Accel. Beams **3**, 094201 (2000).
[20] O. A. Anderson, Part. Accel. **21**, 197 (1987).
[21] T. P. Wangler, K. R. Crandall, R. Ryne, and T. S. Wang, Phys. Rev. ST Accel. Beams **1**, 084201 (1998).
[22] S. Y. Tochitsky, R. Narang, C. V. Filip, P. Musumeci, C. E. Clayton, R. B. Yoder, K. A. Marsh, J. B. Rosenzweig, C. Pellegrini, and C. Joshi, Phys. Rev. Lett. **92**, 095004 (2004).
[23] R. J. England, P. Musumeci, R. Yoder, and J. B. Rosenzweig, in *Proceedings of the 2003 Particle Accelerator Conference, Portland, OR* (IEEE, Piscataway, NJ, 2003), p. 3258.
[24] S. G. Anderson *et al.*, in *Proceedings of the 2001 Particle Accelerator Conference, Chicago* (IEEE, Piscataway, NJ, 2001), p. 89.
[25] A. Murokh, J. B. Rosenzweig, M. Hogan, H. Suk, G. Travish, and U. Happek, Nucl. Instrum. Methods Phys. Res., Sect. A **410**, 452 (1998).
[26] A. Murokh, Ph.D. thesis, University of California, Los Angeles, 2002.
[27] F. Ciocci, L. Giannessi, A. Marranca, L. Mezi, and M. Quattromini, Nucl. Instrum. Methods Phys. Res., Sect. A **393**, 434 (1997).
[28] S. G. Anderson, J. B. Rosenzweig, G. P. LeSage, and J. K. Crane, Phys. Rev. ST Accel. Beams **5**, 014201 (2002).
[29] T. Shaftan, L. Carr, H. Loos, B. Sheehy, W. Graves, Z. Huang, and C. Limborg, in *Proceedings of the 2003 Particle Accelerator Conference, Portland, OR* (Ref. [23]), p. 329.
[30] R. W. Schoenlein, W. P. Leemans, A. H. Chin, P. Volfbeyn, T. E. Glover, P. Balling, M. Zolotorev, K.-J. Kim, S. Chattopadhyay, and C. V. Shank, Science **274**, 236 (1996).
[31] W. P. Leemans, R. W. Schoenlein, P. Volfbeyn, A. H. Chin, T. E. Glover, P. Balling, M. Zolotorev, K. J. Kim, S. Chattopadhyay, and C. V. Shank, Phys. Rev. Lett. **77**, 4182 (1996).
[32] A. Ting *et al.*, Nucl. Instrum. Methods Phys. Res., Sect. A **375**, ABS68 (1996).

[33] I. V. Pogorelsky *et al.*, Phys. Rev. ST Accel. Beams **3**, 090702 (2000).
[34] I. Sakai *et al.*, Phys. Rev. ST Accel. Beams **3**, 090702 (2000).
[35] M. E. Hernandez, Ph.D. thesis, Stanford University, 2003.
[36] J. B. Rosenzweig and G. P. LeSage, in *Advanced Accelerator Concepts: Eighth Workshop*, edited by W. Lawson, AIP Conf. Proc. No. 472 (AIP, New York, 1999), p. 795.
[37] J. Lim, P. Frigola, J. Rosenzweig, S. Telfer, G. Travish, W. Brown, and A. Tremaine, in *Proceedings of the 2003 Particle Accelerator Conference, Portland, OR* (Ref. [23]), p. 2192.
[38] L. Palumbo *et al.*, in *Proceedings of the 2003 Particle Accelerator Conference, Portland, OR* (Ref. [23]), p. 3285.
[39] U. Happek (private communication).